

3D Simulations of M 7 Earthquakes on the Wasatch Fault, Utah, Part II: Broadband (0–10 Hz) Ground Motions and Nonlinear Soil Behavior

by D. Roten,* K. B. Olsen, and J. C. Pechmann

Abstract We predict broadband (BB, 0–10 Hz) ground motions for M 7 earthquakes on the Salt Lake City segment of the Wasatch fault (WFSLC), Utah, which include the effects of nonlinear site response. The predictions are based on low-frequency (LF, 0–1 Hz) finite-difference (FD) simulations for six different rupture models generated during a previous study (Roten *et al.*, 2011), which we combine with high-frequency (HF, 1–10 Hz) shear-to-shear (S-to-S) back-scattering operators to generate BB synthetics. Average horizontal spectral accelerations at 5 and 10 Hz (0.2-s SAs and 0.1-s SAs, respectively) calculated from the linear BB synthetics exceed estimates from four recent ground-motion prediction equations (GMPEs) at near-fault (<5 km) locations on the sediment by more than one standard deviation, but agree with the GMPEs at larger rupture distances. The overprediction of the near-fault GMPE values is largely eliminated after corrections of the BB synthetics for nonlinear soil effects are applied, reducing the SAs from the simulations by up to 70%. These corrections are based on amplitude-, frequency-, and site-dependent correction functions from 1D nonlinear simulations at ~450 locations in the Salt Lake basin, using a simple soil model based in part on published laboratory experiments on Bonneville clay samples. We obtain geometric mean 1-s SAs from from the six scenarios of more than 0.75g on the hanging-wall side of the fault. Geometric mean 0.2-s SAs exceed 1g on the hanging-wall and on the footwall sediments in the central Salt Lake basin, and peak horizontal ground accelerations range from 0.45 to >0.60g in the same general locations.

Online Material: Table of coefficients and amplitude-dependent correction functions for nonlinear soil effects, and figures showing maps of SAs at various frequencies, PGA and PGV, with and without correction for nonlinear soil effects, results of 1D nonlinear simulations, and comparison to ground motion prediction equations.

Introduction

The Salt Lake City segment of the Wasatch normal fault (WFSLC; Fig. 1) in Utah produces M 7 earthquakes with an average return interval of 1350 ± 200 years; the last such event occurred 1230 ± 60 years ago (e.g., Black *et al.*, 1995; McCalpin and Nishenko, 1996). An event of this magnitude, estimated to have an occurrence probability of 16% during the next 100 years (McCalpin and Nelson, 2000) and 6%–9% during the next 50 years (Wong, Silva, Olig, *et al.*, 2002), could have enormous consequences for the Salt Lake City, Utah, metropolitan area. It is imperative to gain a quantitative understanding of the ground motions expected in the Salt Lake basin during a future M 7 event on the WFSLC, as GMPEs are poorly constrained at near-source locations for

normal-faulting $M > 6$ earthquakes. In a previous paper (Roten *et al.*, 2011), we presented simulation results for six M 7 scenario earthquakes on the WFSLC for frequencies of up to 1.0 Hz. In this follow-up study, we extend the analysis to 10 Hz by combining our low-frequency (LF; 0–1 Hz) synthetics with a high-frequency (HF; 1–10 Hz) component based on scattering theory. We also perform simulations of nonlinear soil response, which typically becomes important at higher frequencies, for sites on three cross-basin profiles and use the results to correct our maps of ground-motion parameters.

Background

Three-dimensional numerical simulations are used to model the dynamic fault rupture process and the resulting

*Now at: Swiss Seismological Service, ETH Zürich, Switzerland.

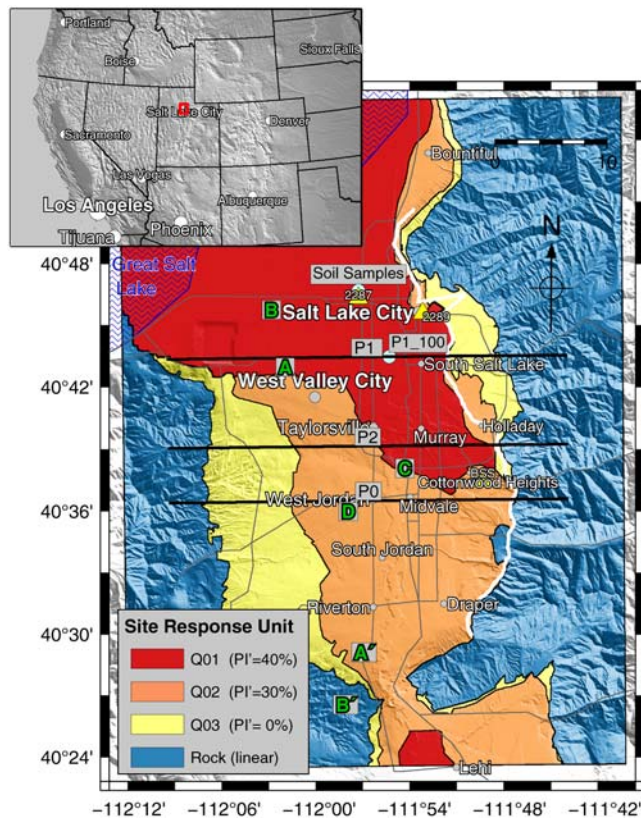


Figure 1. Map of the Salt Lake basin showing the distribution of site response units inside the computational area and the locations of the three cross sections used for nonlinear simulations. The thick white line along the Wasatch front represents the surface rupture of the WFSLC. Bold letters represent the epicenter locations in the six rupture models. Modified from McDonald and Ashland (2008). The color version of this figure is available only in the electronic edition.

seismic wave propagation in strongly heterogeneous media, providing a deterministic characterization of the ground motions during scenario earthquakes (e.g., O'Connell *et al.*, 2007; Olsen *et al.*, 2009). However, these simulations are computationally expensive and therefore typically limited to maximum frequencies of ~ 1 Hz. Recently, increases in the computational resources available to science have allowed this limit to be extended to higher frequencies. Cui *et al.* (2010), for example, simulated an M_w 8 earthquake on the southern San Andreas fault for frequencies up to 2.0 Hz using a minimum shear-wave velocity of $400 \text{ m} \cdot \text{s}^{-1}$. But even the fastest supercomputers available today cannot deterministically simulate ground motion for the whole 0–10 Hz frequency range that is relevant for engineering. Moreover, the geophysical properties of the medium and the earthquake source are usually not known to the detail required for deterministic simulations at frequencies greater than ~ 1 Hz. For this reason broadband (BB) methods have been developed that combine deterministic LF ground motions with a HF component to generate synthetic seismograms for the entire frequency range of engineering interest.

A number of methods use stochastic seismograms to generate the HF component of the signal (e.g., Pitarka *et al.*, 2000; Mena *et al.*, 2006). Other methods incorporate the physics of wave scattering at frequencies above 1 Hz to simulate the HF ground motions (e.g., Zeng *et al.*, 1995; Hartzell *et al.*, 2005). Mai *et al.* (2010) combined HF (1–10 Hz) shear-to-shear (S-to-S) back-scattering seismograms with LF (0–1 Hz) deterministic seismograms for the 1994 Northridge earthquake and found that the resulting BB synthetics were consistent with observations for the modeled frequency range. Mena *et al.* (2010) developed the method further by incorporating dynamically consistent source-time functions and accounting for finite-fault effects in the computation of the HF waveforms. Their method also includes corrections for local site effects that use frequency- and amplitude-dependent amplification functions (Borcherdt, 1994).

Deterministic 3D LF simulations typically do not take soil nonlinearity into account, because this effect is usually not very important at frequencies below 1 Hz. For the HF component of the ground motion, however, nonlinear soil behavior may become an important factor during strong earthquakes. Simulations of 0–10 Hz of wave propagation in nonlinear media are primarily limited to 1D (e.g., Hartzell *et al.*, 2004) and 2D (e.g., Bonilla *et al.*, 2006). In geotechnical engineering it is standard practice to apply an equivalent linear 1D model (e.g., Schnabel *et al.*, 1972). It is well accepted that this physical model is limited to a certain strain level above which the soil behavior becomes very complex. In these cases a fully nonlinear calculation needs to be performed in order to accurately estimate the soil response.

The most recent and complete studies predicting BB ground motions for M 7 scenario earthquakes on the WFSLC were performed by Wong, Silva, Olig, *et al.* (2002) and Solomon *et al.* (2004), who produced maps of average expected peak ground acceleration (PGA) and spectral acceleration (SA) at periods of 0.2 s and 1 s (0.2-s SAs and 1-s SAs, respectively) in and around the Salt Lake basin. Their methods were based on a combination of ground-motion attenuation relationships and stochastic modeling. To account for site effects and nonlinear soil behavior, Wong, Silva, Olig, *et al.* (2002) and Solomon *et al.* (2004) defined five generalized site response units (SRUs) and calculated 1D amplification factors for each unit as a function of input PGA and unconsolidated sediment thickness. Shear modulus reduction and hysteretic damping were incorporated using an equivalent-linear formulation (Silva *et al.*, 1998). The M 7 scenario earthquake ground-motion maps by Wong, Silva, Olig, *et al.* (2002) and Solomon *et al.* (2004) show the highest PGAs and 0.2-s SAs near the surface break on the footwall side in the central Salt Lake basin and on the hanging-wall side in the southern part of the Salt Lake basin. These areas are covered by stiff deposits of mostly gravel and sand, which in their models amplify the ground motions at higher frequencies. Sites on the hanging-wall side of the fault that are underlain by soft lacustrine and alluvial silts, clays, and sands exhibit lower ground motions due to damping by nonlinear soil

response. For a period of 1 s, Wong, Silva, Olig, *et al.* (2002) and Solomon *et al.* (2004) predict the largest ground motions at near-fault sites on deep hanging-wall sediments in the southern Salt Lake basin as well as on shallow footwall sediments in the central Salt Lake basin (up to 1.3–1.5g).

Recently Roten *et al.* (2011) used 3D finite-difference (FD) simulations of wave propagation to estimate 0–1 Hz ground motions in the Salt Lake basin. These simulations, performed for six different scenarios produced by spontaneous rupture modeling, predict that the highest 2-s SAs and 3-s SAs will occur on the deep sediments on the hanging-wall site of the fault, with the locations of the peak SAs controlled by constructive interference between the direct *S* wave and surface waves generated at the basin edges. However, these simulations were limited to frequencies below 1 Hz. Therefore, it was not possible to compute SAs at 1 s or shorter periods from these synthetics, prohibiting a direct comparison with the higher-frequency simulations of Wong, Silva, Olig, *et al.* (2002) and Solomon *et al.* (2004). Nevertheless, the findings by Roten *et al.* (2011) are consistent with 3D simulations performed for the structurally comparable Teton (Wyoming) fault and nearby sedimentary basin (O’Connell *et al.*, 2007).

The results of Wong, Silva, Olig, *et al.* (2002) and Solomon *et al.* (2004) suggest that the simulated ground-motion pattern changes at higher frequencies during strong ground motion, as they predict the largest PGAs and 0.2-s SAs in the central Salt Lake basin to be on the footwall. However, studies of site amplification from weak motion records of nuclear explosions in the period range 0.2 s–0.7 s (e.g., Williams *et al.*, 1993) found the highest amplification on the hanging-wall side of the fault, where the sediments are deepest. This discrepancy is likely related to nonlinear damping in the soil during strong ground motion. The purpose of this study is to produce BB synthetics based on the

simulations of Roten *et al.* (2011), and including nonlinear soil response, in order to produce ground-motion synthetics useful for structural engineers and to allow a direct comparison with the results of Wong, Silva, Olig, *et al.* (2002) and Solomon *et al.* (2004).

Methodology for Computing BB Ground Motions

We used a four-step method to generate BB synthetics, including nonlinear site response, for an *M* 7 event on the WFSLC. Figure 2 shows a flow chart summarizing the input parameters, tools, and products of the method. The first two steps, spontaneous rupture simulation (Dalguer and Day, 2007) and 3D wave propagation (Olsen, 1994), were discussed in detail in Roten *et al.* (2011). Here we present the results of steps three and four. We follow the method of Mai *et al.* (2010) and Mena *et al.* (2010) to calculate the HF component of ground motion. Additionally, we calculate nonlinear soil response for ~450 sites in the Salt Lake basin with the nonlinear, anelastic hysteretic FD code NOAH (Bonilla *et al.*, 2005).

LF (0–1 Hz) Ground Motion

Roten *et al.* (2011) simulated the ground motion for six kinematic source models. The kinematic sources were generated by projecting slip rate histories, obtained from spontaneous rupture simulations on a planar, vertical fault, onto a 3D dipping model of the Wasatch fault. The ensemble of six *M* 7 scenario earthquakes has a representative distribution of hypocenter locations (Fig. 1), placed near the three nonconservative slip barriers (i.e., fault irregularities where a change occurs in the direction of the slip vector) of the WFSLC interpreted by Bruhn *et al.* (1992). Source models A and B nucleate near the northern barrier and A’ and B’ near the southern barrier. Models C and D have hypocenters near

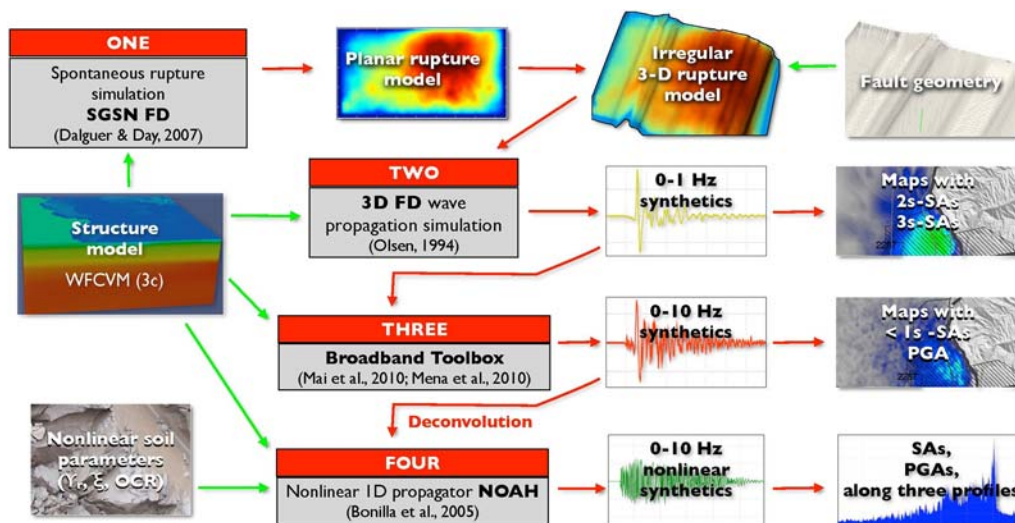


Figure 2. Flow chart summarizing the four stages in generating BB synthetics including nonlinear soil behavior. The color version of this figure is available only in the electronic edition.

the central nonconservative barrier of the fault segment. The 3D wave propagation simulations revealed strong along-strike rupture directional effects for unilateral rupture, as well as significant amplification by the deep sediments on the hanging-wall side of the fault. To characterize the spatial variability of ground motions at higher frequencies, we generate BB synthetics and perform nonlinear site response simulations for all six of the $M_w 7$ scenarios simulated by [Roten et al. \(2011\)](#).

Generation of BB Synthetics

In the BB method of [Mai et al. \(2010\)](#), the generation of the HF part of the seismogram is based on multiple S-to-S back-scattering theory. [Zeng et al. \(1991\)](#) provide a compact integral solution of the scattered wave energy equation for an unbounded 3D medium, which quantifies the energy envelope E of the S-to-S scattered waves:

$$E(\mathbf{r}, t) = \frac{\delta(t - \frac{r}{v_s})e^{-\eta v_s t}}{4\pi v_s r^2} + \sum_{n=1}^2 E_n(\mathbf{r}, t) + \int_{-\infty}^{+\infty} \frac{e^{i\Omega t}}{2\pi} d\Omega \times \int_0^\infty \frac{(\frac{\eta_s}{k})^3 [\tan^{-1}(\frac{k}{\eta + i\Omega/v_s})]^4 \sin(kr)}{2\pi^2 v_s r [1 - \frac{\eta_s}{k} \tan^{-1}(\frac{k}{\eta + i\Omega/v_s})]} dk. \quad (1)$$

In equation (1), \mathbf{r} is the source–receiver vector, t is time, and v_s is the average S -wave velocity between the source and the receiver. The total S -wave attenuation coefficient $\eta = \eta_i + \eta_s$ contains the scattering coefficient η_s and the intrinsic attenuation coefficient η_i ; we use $\eta_s = \eta_i = 0.03 \text{ km}^{-1}$ in this study. The first two terms in equation (1) represent time-domain solutions for the direct arrival and the first- and second-order scattered wave energy (E_1 and E_2 , see [Zeng et al., 1991](#)). The third term represents the sum of the higher-order ($n \geq 3$) scattered wave energy, where $i\Omega$ denotes the Fourier transform variable with respect to time, and k is the wavenumber. [Zeng \(1993\)](#) shows that the wave field of scattered P and S waves is dominated by multiple S-to-S back-scattered body waves described in equation (1). Scattered surface waves are not explicitly considered with this approach.

To generate a site-specific scattering Green's function, the code of [Mai et al. \(2010\)](#) generates a series of random scattering wavelets with uniformly distributed amplitudes between $\pm\sqrt{3}$, which assures a mean wave energy of unity ([Zeng et al., 1995](#)). These wavelets are then multiplied with the envelope of the scattered wave energy (equation 1), with P - and S -wave arrival times for each site computed from a 3D raytracing method. For the raytracer we used the same velocity model as for the 3D FD simulations, downsampled to a spatial resolution of 1 km. Additionally, the code models site-specific attenuation in the upper layers with a kappa coefficient, κ . For our BB simulations in the Salt Lake basin, we used $\kappa = 0.03 \text{ s}$ ([Wong et al., 2011](#)).

Because the point source approximation by [Mai et al. \(2010\)](#) is not appropriate for modeling an $M_w 7$ event on the WFSLC, we employ the extended fault approximation

developed by [Mena et al. \(2010\)](#) for the generation of BB synthetics. We divide the WFSLC fault model into 925 sub-faults with a unit rupture area of 1 km^2 and a uniform slip of 1 cm each. The BB generator adds the contribution of each subfault to obtain the total HF ground motion $A(t)$ based on the empirical Green's function method of [Irikura and Kamae \(1994\)](#):

$$A(t) = \sum_{i=1}^{N^2} (r/r_i) \text{STF}(t - t_i) * C \times \text{SGF}(t). \quad (2)$$

In this expression, r is the hypocentral distance, N^2 is the total number of subfaults, and r_i is the distance of the observation point to the i -th subfault. The operator $*$ indicates convolution. $\text{STF}(t)$ is the source–time function, $\text{SGF}(t)$ is the scattering Green's function, and C is the stress-drop ratio between the small and large events. The level of the HF spectral amplitude is scaled depending on the seismic moment M_0 using the following scaling law ([Mena et al., 2010](#)):

$$\frac{M_0}{m_0} = \text{CN}^3, \quad (3)$$

where m_0 is the seismic moment of the subfaults. The time t_i in equation (2) accounts for the time delay for rupture propagation along the fault

$$t_i = \frac{r_i}{v_s} + \frac{\xi_i}{v_r}, \quad (4)$$

where ξ_i is the distance from the subfault to the hypocenter, v_s is the shear-wave velocity, and v_r is the rupture velocity. [Mena et al. \(2010\)](#) employ an STF introduced by [Dreger et al. \(2007\)](#) due to its smooth spectrum, modified to include a healing phase.

The LF FD synthetics are combined with the HF scattering operators (maximum frequency 20 Hz) using a simultaneous amplitude- and phase-matching algorithm ([Mai and Beroza, 2003](#)). This approach finds the optimum matching frequency within a predefined frequency band and minimizes mismatches in both amplitude and phase. The matching frequency depends on the site and component. In this work we search for a matching frequency between 0.8 and 1.0 Hz, because our LF synthetics are limited to 1.0 Hz. We apply the scattering operators to LF synthetics at every fifth node on the surface of the computation grid. This results in a spatial resolution of 200 m and a grid dimension of 225×300 nodes (67,500 sites), which allows us to generate SA and PGA maps with sufficient resolution.

Calculation of Nonlinear Soil Response

We use the second-order accurate, staggered-grid 1D finite difference code NOAH ([Bonilla et al., 2005](#)) to model SH wave propagation in soil columns of 240 m depth. The datum of 240 m was chosen in order to include the structure

above the R_1 interface, which marks the transition from unconsolidated to semiconsolidated sediments in the Salt Lake basin (Hill *et al.*, 1990). The nonlinear simulations are performed for 540 sites, which are distributed evenly along three profiles across the Salt Lake basin (Fig. 1) at 200 m intervals.

Soil Model. NOAH uses the hyperbolic soil model (Hardin and Drnevich, 1972), which can be prescribed in different ways. It is able to treat undrained conditions of effective stress using the multispring mechanism model introduced by Towhata and Ishihara (1985), and an extension of this model that treats cyclic mobility and soil dilatancy (Iai *et al.*, 1990a,b). This cyclic mobility model uses a relatively large number of variables (five dilatancy parameters), which need to be determined from laboratory tests that include pore pressure generation (e.g., Bonilla, 2001; Roten *et al.*, 2009). Because we only have laboratory data from one site in our computational area, we decided against simulating pore pressure generation in this study and use the NOAH code for total stress analysis. In this configuration the multispring model gives the same result as a single-element hyperbolic model following the generalized Masing rules (Bonilla, 2000); it is very similar to the nonlinear model NOAHH described in Hartzell *et al.* (2004).

In the hyperbolic model, the reduction of the shear modulus G with increasing strain γ_{xy} is described by

$$\frac{G}{G_0} = \frac{1}{1 + \frac{\gamma_{xy}}{\gamma_r}}, \quad (5)$$

where G_0 is the maximum shear modulus. The reference strain γ_r is defined as

$$\gamma_r = \frac{\tau_0}{G_0}, \quad (6)$$

where τ_0 is the maximum shear stress that the material can support in the initial state. The nonlinear relation between stress τ_{xy} and strain γ_{xy} is described by a backbone curve during initial loading (Fig. 3):

$$F_{bb}(\gamma_{xy}) = \tau_0 \frac{\frac{\gamma_{xy}}{\gamma_r}}{1 + \left| \frac{\gamma_{xy}}{\gamma_r} \right|}. \quad (7)$$

Subsequent loading and unloading cycles are expressed as

$$\frac{\tau_{xy} - \tau_t}{\kappa_H} = F_{bb} \left(\frac{\gamma_{xy} - \gamma_t}{\kappa_H} \right), \quad (8)$$

where the coordinates (γ_t, τ_t) denote the reversal points in the strain-stress space (Fig. 3). The hysteresis scale factor κ_H controls the shape of the loop (Bonilla *et al.*, 1998), and κ_H equals 2 in the original Masing (1926) formulation. In the extended Masing rules (e.g., Pyke, 1979; Vucetic, 1990; Li and Liao, 1993), this constraint on κ_H is released to prevent the computed stress from exceeding the maximum strength τ_0 of the material. Bonilla (2000) generalized the Masing

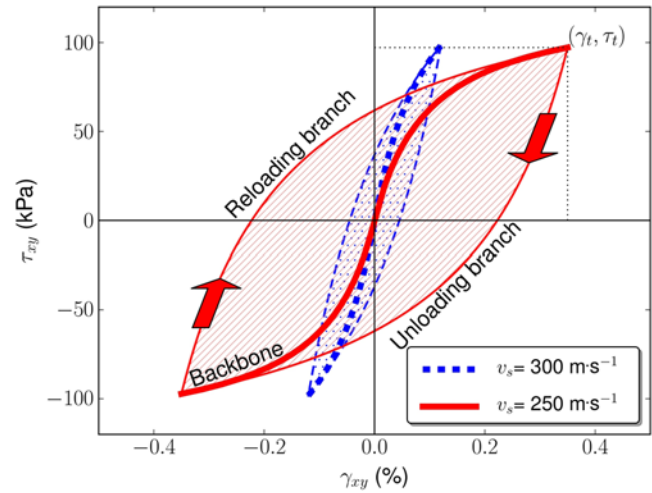


Figure 3. Typical shear stress-strain relationship of soil under cyclic loads for a hyperbolic model. Backbone and reloading curves were computed from equations (7) and (8) ($\kappa_H = 2$) using a reference strain γ_r of 0.1% and two different values for the shear modulus G_0 , corresponding to shear-wave velocities of 250 and 300 $\text{m} \cdot \text{s}^{-1}$ and a density of 2000 $\text{kg} \cdot \text{m}^{-3}$. The pair (γ_t, τ_t) represent the point where the path reverses from loading to unloading. Modified from Bonilla (2001). The color version of this figure is available only in the electronic edition.

rules further by defining a variable hysteresis scale factor κ_H that assures that the stress-strain path during each loading/reloading is bounded by the maximum shear strength τ_0 . This hysteresis formulation was named the generalized Masing rules because it includes the Cundall–Pyke hypothesis (Pyke, 1979) and Masing’s original formulation as special cases.

In the hyperbolic model the damping ratio approaches $2/\pi$ ($\sim 64\%$) at large strains (Ishihara, 1996), which is much larger than the damping ratio of 25%–40% observed in experimental data. Ishihara *et al.* (1985) suggested a method to control the damping ratio by computing a new backbone curve, which follows a hysteresis path controlled by the required damping ratio. The required strain-dependent damping ratio ξ_H is calculated with the following expression (Hardin and Drnevich, 1972):

$$\xi_H = \frac{\frac{\gamma_r}{\gamma_r}}{1 + \left| \frac{\gamma_{xy}}{\gamma_r} \right|} \xi_{\max}, \quad (9)$$

where γ_{xy} is the level of deformation, and ξ_{\max} is the maximum damping ratio at large strains. By equating ξ_H in equation (9) with the damping ratio from the hyperbolic model, NOAH finds a solution for the reference strain γ_r' that is compatible with the desired damping value ξ_H . This new reference strain γ_r' is then used to recompute the backbone curve, and the procedure is repeated for each time step. In addition to hysteretic damping, NOAH models intrinsic attenuation with constant Q by the rheology of the generalized Maxwell body (Day, 1998). For a more detailed description of the model refer to Bonilla (2001).

In the original NOAHH code, the maximum shear stress τ_0 for the backbone curve (equation 7) is calculated from the angle of internal friction φ and cohesion c (Hartzell *et al.*, 2004) using the Mohr–Coulomb failure criterion (e.g., Jaeger *et al.*, 2007):

$$\tau_0 = \sigma_m \sin(\varphi) + c \cos(\varphi) \quad \sigma_m = \sigma_v \frac{1 + K_0}{2}, \quad (10)$$

where σ_m is the effective mean stress, σ_v is the vertical effective stress, and K_0 is the coefficient of Earth at rest. For the nonlinear simulations in the Salt Lake basin, we prefer not to use this method, as we have little information about the parameters c and φ . Instead, we modified the code to require γ_r instead of c as the soil parameter, and we calculate τ_0 directly from γ_r using equation (6) (L.F. Bonilla, personal comm., 2009). Therefore, we need two nonlinear parameters for each layer: the reference strain γ_r and the maximum damping ratio ξ_{\max} .

Soil Parameters. We extract the P -wave velocity v_P , the low-strain S -wave velocity v_S , and the density ρ from version 3c of the Wasatch Front Community Velocity Model (WFCVM; Magistrale *et al.*, 2009), which is also the model used for the LF FD simulations of Roten *et al.* (2011). For each site along the three profiles we extract v_P , v_S , and ρ at a vertical spacing of 1 m (without constraining the velocities to a minimum value, as is often necessary for FD simulations due to computational limitations). The quality factors Q_P and Q_S are computed from v_S (in $\text{km} \cdot \text{s}^{-1}$) using an empirical relation derived by Brocher, (2006):

$$Q_S = \begin{cases} 13 & v_S < 0.3 \text{ km} \cdot \text{s}^{-1} \\ -16 + 104.13 v_S - 25.22 v_S^2 + 8.21 v_S^3 & v_S \geq 0.3 \text{ km} \cdot \text{s}^{-1} \end{cases} \quad (11)$$

$$Q_P = 2Q_S.$$

Bay and Sasanakul (2005) performed resonant column and torsional shear tests on Bonneville clay soil samples collected at four different sites around the Wasatch front. The only sampling location that is within our computational domain is the Brigham Young University research site northwest of Salt Lake City International Airport (labeled soil samples in Fig. 1). Bay and Sasanakul (2005) concluded that the Bonneville soils exhibit more linear behavior, that is, a smaller modulus reduction and less damping, than would be predicted by commonly used empirical relationships (e.g., Vucetic and Dobry, 1991; Darendeli, 2001). To correct for this increased linearity they propose using a modified plasticity index (PI), which is 10% higher than the actual PI, for the relation of Vucetic and Dobry (1991). For the relationship of Darendeli (2001), Bay and Sasanakul (2005) suggest using a modified plasticity index PI' , predicted with the following linear relation:

$$PI' = 1.8956 PI + 25.92\%. \quad (12)$$

For example, a PI of 2% was measured on the sample SLC35, extracted near Salt Lake City airport at a depth of 10.7 m. However, the best match between the observed and predicted modulus reduction and damping curves was obtained when using $PI' = 30\%$ in Darendeli's relationship. We follow these recommendations and use the empirical relationships of Darendeli (2001) to predict γ_r and ξ_{\max} from PI' and other parameters.

To assign a value for the modified plasticity index PI' to each site along the three profiles we use the Quaternary SRUs (Fig. 1) mapped by McDonald and Ashland (2008). Table 1 summarizes the properties of the different SRUs and the values of PI' assigned to them. The clay-rich composition of unit Q01 is reflected in the rather high PI' of 40%. Q02 has more silt, so a lower value of 30% was used for PI' . The lacustrine and alluvial deposits on the footwall of the Wasatch fault consist mostly of gravel and sand with little clay content. Thus, $PI' = 0\%$ was used for SRU Q03 (James Bay, personal comm., 2009). Sites outside the basin, which are classified as Tertiary (T), Mesozoic (M), or Paleozoic or Precambrian (P) bedrock, are treated as fully linear.

Darendeli (2001) proposed the following relation to predict the reference strain as a function of overconsolidation ratio (OCR), plasticity index (PI'), and confining pressure (σ_0):

$$\gamma_r = (\phi_1 + \phi_2 \times PI' \times OCR^{\phi_3}) \sigma_0^{\phi_4}. \quad (13)$$

We followed Bay and Sasanakul (2005) and assumed normal consolidation ($OCR = 1$) for all units; consequently, we used $K_0 = 0.5$ for the coefficient of Earth at rest in NOAH. The constants ϕ_1 , ϕ_2 , ϕ_3 , and ϕ_4 are given in Darendeli (2001, table 8.12). We determined the reference strain at 1 m

Table 1
Site Response Units, Modified Plasticity Index (PI'),
and Average V_{S30}

Unit (s)	Description (McDonald and Ashland, 2008)	PI'	$\overline{V_{S30}}$ ($\text{m} \cdot \text{s}^{-1}$)
Q01	Lacustrine and alluvial silt, clay and fine sand; alluvial, lateral-spread, or marsh deposits typically overlie lacustrine deposits	40%	250
Q02	Lacustrine sand and gravel; interbedded lacustrine silt, clay, and sand; latest Pleistocene to Holocene alluvial fan deposits	30%	375
Q03	Lacustrine and alluvial gravel and sand; pre-Bonneville alluvial fan deposits, primarily where they occur on the footwall of the Wasatch fault	0%	507
T, M, P	Tertiary, Mesozoic, Paleozoic, or Precambrian rock; treated as linear	–	–

depth intervals, assuming an average depth to the groundwater table of 3 m to calculate σ_0 . Additionally, we evaluated the modulus reduction curve and its standard deviation σ using Darendeli's equations. By adding or subtracting σ from these modulus reduction curves and determining the strain where $G/G_0 = 0.5$, we defined an upper and lower value for the reference strain $\gamma_r \pm \sigma$. We also computed the damping curve at each depth interval of 1 m and used the maximum to define the parameter ξ_{\max} . The equations for the damping curves are given in Darendeli (2001), and they require a frequency f and the number of cycles N ; we used $f = 1$ Hz and $N = 10$. We also took the standard deviation of the damping ratio into account and determined $\xi_{\max} \pm \sigma_d$. The maximum damping ratios we obtained with this method vary between $\sim 25\%$ near the surface and $\sim 20\%$ at depth, with a standard deviation of 3%–4%.

Figure 4 shows γ_r increasing with depth for a typical location on site response unit Q01 (site 100 along P_1). The R_1 interface at this site is located at a depth of ~ 210 m, and it is accompanied by a sharp velocity contrast, with v_s increasing from 500 to 914 $\text{m} \cdot \text{s}^{-1}$. We defined layers with a shear-wave velocity below 750 $\text{m} \cdot \text{s}^{-1}$ as nonlinear and the remaining layers as linear. The reference strain was formally set to 1% for the linear part of the structure in Figure 4, even though γ_r is only used for nonlinear layers in NOAH.

The symbols in Figure 4 show the reference strain determined from the Bonneville clay soil samples at different confining pressures. Because the reference strain determined from the soil samples shows large variability with the sampling location, we generate two additional nonlinear models for each site, representing the upper and lower bound on nonlinearity. The lower-bound nonlinear model is obtained by using $\gamma_r + \sigma$ for the reference strain and $\xi_{\max} - \sigma_d$ for the maximum damping ratio. Conversely, the upper bound nonlinear model uses $\gamma_r - \sigma$ and $\xi_{\max} + \sigma_d$ for the reference strain and maximum damping ratio, respectively. The dashed lines in Figure 4 show the $\gamma_r \pm \sigma$ as a function of depth. We perform nonlinear simulations with all three models to estimate the sensitivity of the final ground motion to uncertainties in the soil parameters.

Finite Difference Parameters. Nonlinear soil effects may decrease the shear-wave velocity during strong shaking, demanding a decrease in the grid step as compared with linear simulations. NOAH comes with a helper program that computes the required spatial step Δx and temporal discretization Δt to meet the stability criteria

$$\Delta x = \frac{v_{s,\min}}{f_{\max} n}, \quad (14)$$

and

$$\Delta t = p_0 \frac{\Delta x}{v_{s,\max}}, \quad (15)$$

where p_0 is a fraction of the minimum Δt needed to satisfy the stability condition, n is the number of grid points per

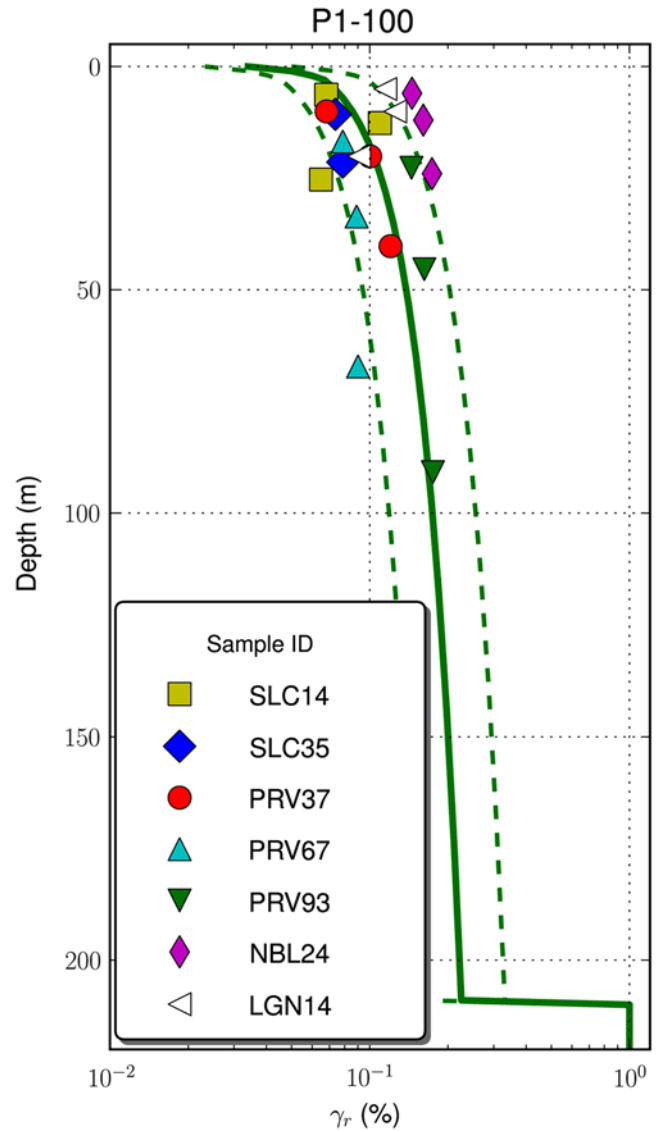


Figure 4. Reference strain γ_r (solid line) and $\gamma_r \pm \sigma$ (dashed lines) as a function of depth derived from Darendeli (2001) for site P1-100 (Fig. 1). The symbols show γ_r determined by Bay and Sanakul (2005) from torsional shear tests at the depth corresponding to the applied confining pressure. The color version of this figure is available only in the electronic edition.

wavelength, and f_{\max} is the maximum simulated frequency. We used $n = 30$ and $p_0 = 0.5$ to ensure numerical stability and selected $f_{\max} = 20$ Hz to cover a broad frequency range for the BB simulations. Because the minimum and maximum shear-wave velocity vary with the local geology, different values for the spatial and temporal discretization are used for each site along the three profiles. We simulated 60 s of nonlinear wave propagation, using the entire length of synthetics available from the FD and BB simulations.

Boundary Conditions and Input Signals for Nonlinear Simulations. We apply a deconvolution to the surface BB synthetics to obtain a signal that represents the wave field at a depth of 240 m, where the base of the soil column used for

the 1D nonlinear simulations is located. For the deconvolution we use the top 240 m in the velocity model that was employed for the 3D LF simulations. Because the latter differs from the 1D nonlinear model in resolution and minimum v_s , we also perform a 1D linear simulation for each site along the two profiles in order to ascertain how much of the difference between linear and nonlinear synthetics is related to nonlinearity in the soil model.

NOAH provides two different options for the boundary conditions (BCs) at the base of the soil layer: rigid and elastic. Many numerical studies on nonlinear soil behavior use borehole records as input signals (e.g., [Bonilla et al., 2005](#)). As it is often not possible to separate the upgoing from the downward reflected wave field, downhole records are used in combination with rigid BCs. In this case the motion at the base of the column is prescribed by the borehole signal at any time. This approximation allows no energy to be radiated back into the underlying medium and may produce multiple reflections within the soil column ([Joyner and Chen, 1975](#)). These resonances are naturally avoided if the dissipation within the soil column is large enough, especially in the case of strong nonlinearity.

We tested this approach by deconvolving the BB signal at site P1-100 (Fig. 1) for borehole conditions using a detailed 1D model of the top 240 m, and propagating this signal back to the surface using NOAH in linear mode (Fig. 5a). The resulting ground motion should be identical to the ori-

ginal BB signal under ideal conditions. However, the spectra of the resulting surface acceleration exhibits some strong peaks that were not present in the original BB spectra, with the first peak located near 0.5 Hz. This frequency is very close to the expected resonance frequency of the soil column, which is ~ 0.57 Hz with an average shear-wave velocity of $547 \text{ m} \cdot \text{s}^{-1}$ and 240 m thickness (dashed line in Fig. 5c). Therefore, rigid BCs are not suitable for this study, because we must expect that dissipation will be small at some sites due to limited nonlinearity.

Instead, we decided to use the elastic BCs described by [Joyner and Chen \(1975\)](#) at the base of the soil column. These transmitting BCs allow propagation of waves into the underlying medium, but they require the incident wave field as input signal. We computed the transfer function between the free surface and a model with the top 240 m removed and used it to deconvolve the free-surface BB synthetics. As the resulting signals represent outcrop records, their amplitude was divided by two to obtain the incoming wave field at depth. We verified this method by propagating this signal back to the surface using NOAH with elastic BCs. The signal obtained after the deconvolution and 1D propagation (Fig. 5b,d) is very similar to the original BB input in the time and frequency domains. For this reason we chose transmitting BCs in NOAH, and applied the procedure described previously to find the incoming wave field at depth.

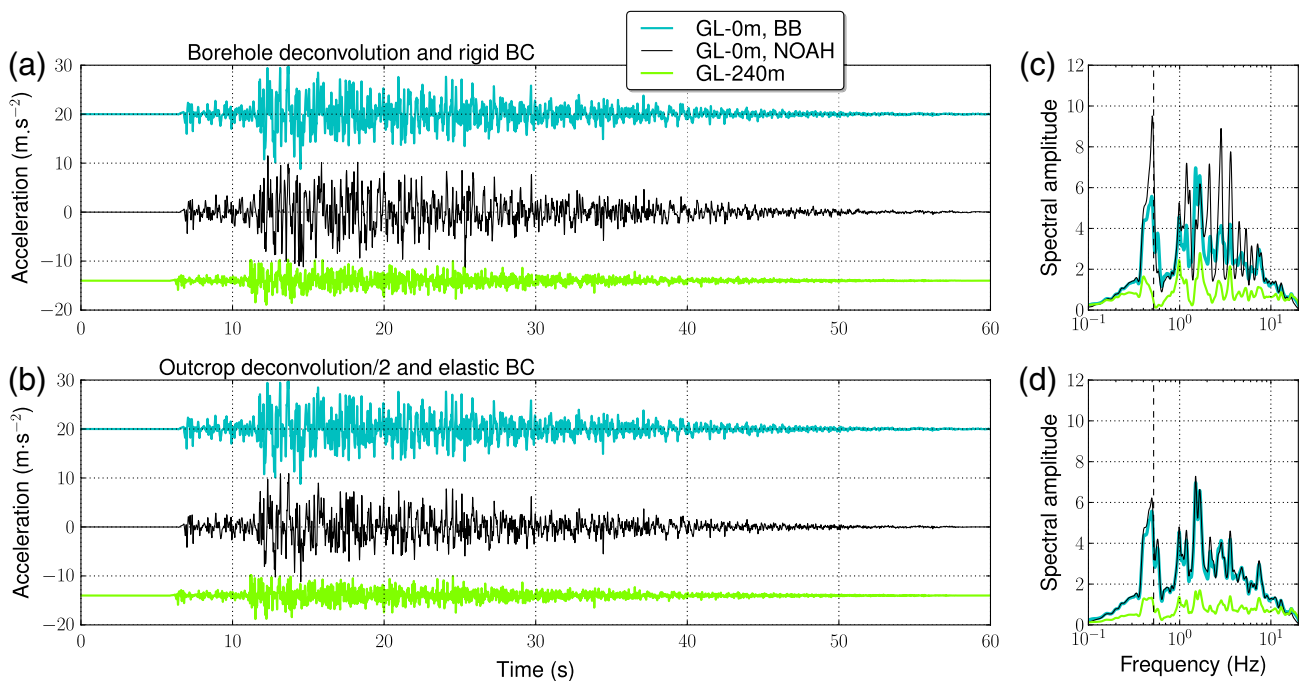


Figure 5. Test of different BCs in NOAH. (a) The panel shows the original BB synthetic on the free surface, which was deconvolved to represent a borehole record at a depth of 240 m and then propagated back to the surface using rigid BCs in NOAH. (b) The panel shows the same experiment, but deconvolving to outcrop conditions of a depth of 240 m, dividing the resulting signal by two, and propagating the result back up to the surface using transmitting (elastic) BCs at a depth of 240 m. (c, d) Fourier spectra were smoothed using the method defined by [Konno and Ohmachi \(1998\)](#) with $b = 40$. The color version of this figure is available only in the electronic edition.

Linear BB Synthetics

Figure 6 shows LF and linear BB synthetic velocity records from scenario earthquake B' in the time and frequency domains at three selected sites. The Fourier spectra of the LF synthetics exhibit a sharp drop-off at frequencies above 1 Hz, while the BB synthetics contain energy up to 20 Hz, with a matching frequency of 0.9 ± 0.1 Hz. The seismograms at sites 2287 (Salt Lake City International Airport) and 2289 (downtown Salt Lake City) are dominated by the surface waves present in the LF synthetics (Roten *et al.*, 2011), which generate horizontal peak ground velocities up to $1.27 \text{ m} \cdot \text{s}^{-1}$ in the east–west direction at site 2287 and up to $1.78 \text{ m} \cdot \text{s}^{-1}$ in the north–south direction at site 2289. The surface waves are less pronounced at the Butlerville substation site (BSS), and consequently the HF component contributed by the scatterograms is more evident.

The BB frequency content of these synthetics allows us to compute spectral accelerations (SAs) at frequencies above 1 Hz. We compute the geometric mean of both horizontal components following a method introduced by Boore *et al.* (2006), which is independent of sensor orientation (GMRotD50). Spectral accelerations shown in this text correspond to the GMRotD50 measure, which represents the median value of geometric means obtained from all possible rotation angles for a given oscillator period.

Figure 7a is a map of spectral accelerations at 5 Hz obtained from linear BB synthetics (BB 0.2-s SAs) for source model B, which nucleates at the northern end of the WFSLC. The small-scale variability in the BB SA maps is caused by the stochastic scattering approach and reflects the random distribution of pointlike scatterers inside the volume. Broadband SAs exceeding $1.5g$ occur at many hanging-wall side locations, especially in the southern part of the Salt Lake basin, but also inside a small patch northwest of the downtown Salt Lake City area. This pattern reflects the distribution of 2-s SAs and 3-s SAs calculated from the FD simulations (Ro-

ten *et al.*, 2011), because the HF scatterograms are scaled to the amplitude of the LF synthetics at the matching frequency.

Figure 7b shows BB 0.2-s SAs for scenario B', which has an epicenter on the southern end of the WFSLC. For this source, the highest BB SAs are encountered mainly in the northern part of the Salt Lake basin, inside a large patch including downtown Salt Lake City, south Salt Lake, and the area southwest of the Wasatch fault stepover near Holladay. These results mimic the strong unilateral rupture direction effects that were found during the LF FD simulations, with stronger ground motions in the downtown Salt Lake City area for ruptures nucleating in the south than for ruptures nucleating in the north (Roten *et al.*, 2011). Amplification effects caused by the deep low-velocity sediments on the hanging-wall side of the fault are also evident in the BB SA maps. Note that the only footwall side location where BB 0.2-s SAs exceed $2.25g$ is located just north of Holladay above the central part of the WFSLC (Fig. 7a). In this area, the WFSLC cuts through the basin fill, running parallel to the Wasatch front at a distance of 3–5 km. As a result, low-velocity sediments are encountered on both sides of the fault in the central Salt Lake basin area. (Ⓢ) The electronic supplement to this article contains spectral acceleration maps based on linear BB synthetics for all six scenarios at 1, 2, 3, 5, and 10 Hz, plus maps of PGA and peak ground velocity [PGV]. See Fig. S1 in the electronic supplement.)

Figure 8 compares BB SAs as a function of distance along two cross sections with SAs predicted by four next-generation GMPEs: Boore and Atkinson (2008), Campbell and Bozorgnia (2008), Abrahamson and Silva (2008), and Chiou and Youngs (2008). In the remainder of this text, we will refer to these next-generation attenuation (NGA) relations as BA08, CB08, AS08, and CY08, respectively. For each site along the two cross sections, we used the 3D fault model and 3D velocity mesh to calculate the rupture distance, R_{Rup} ; the horizontal distance to the top of the rupture, R_x ; the

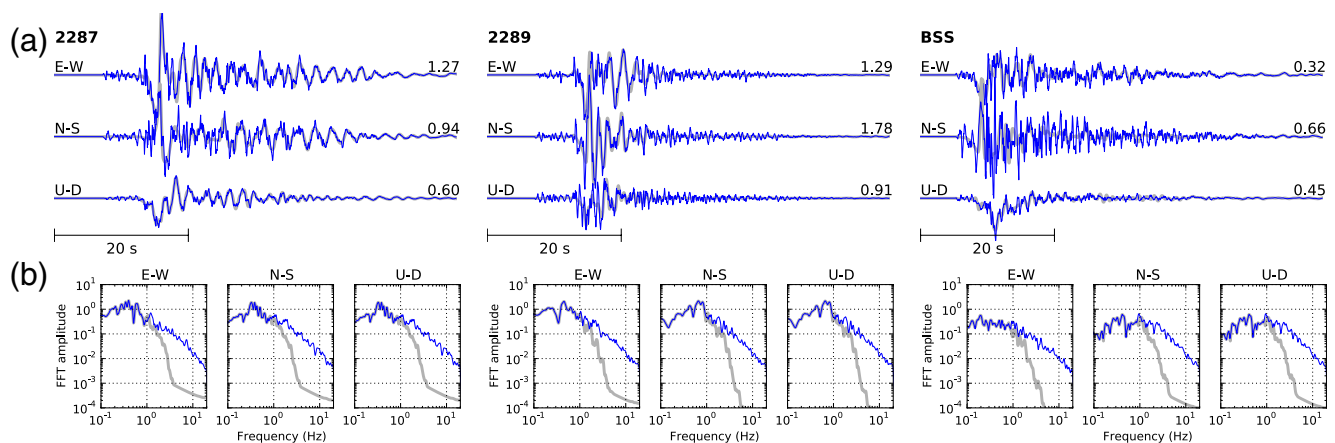


Figure 6. (a) Comparison of LF (thick lines) and BB (thin lines) velocity synthetics and (b) corresponding Fourier spectra for source model B' at three selected strong motion sites in the Salt Lake basin (Fig. 1): Salt Lake City International Airport (2287), downtown Salt Lake City (2289), and Butlerville substation (BSS). A Konno–Ohmachi window ($b = 80$) was used to smooth the Fourier spectra. The numbers on the time-domain records denote peak velocity in $\text{m} \cdot \text{s}^{-1}$. The color version of this figure is available only in the electronic edition.

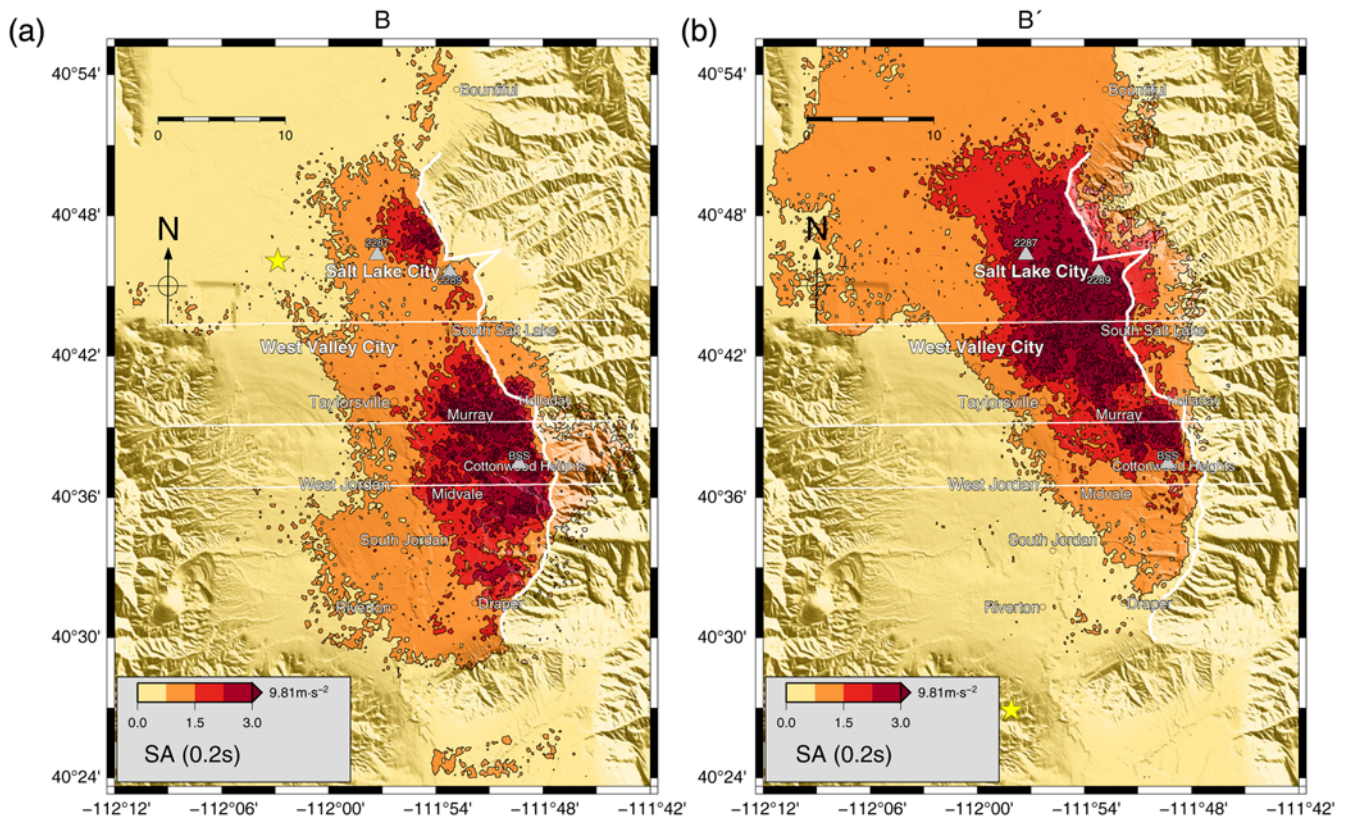


Figure 7. Maps of orientation-independent geometric mean horizontal spectral accelerations obtained from linear BBs based on (a) rupture model B and from (b) rupture model B' at 5 Hz. Stars depict the hypocenters. The thick white line along the Wasatch front represents the surface rupture of the WFSLC. The three cross sections used for nonlinear simulations are indicated by the thin white lines. The color version of this figure is available only in the electronic edition.

horizontal distance to the surface projection of the rupture, R_{JB} ; the average shear-wave velocity in the top 30 m, V_{S30} ; and other site-specific parameters required by the GMPEs.

Figure 8a shows BB 0.2-s SAs along cross-section P0 for rupture model B. The highest accelerations are encountered on the hanging-wall close to the fault, where the SAs predicted by all four GMPEs are exceeded for $R_x < 5$ km. The GMPE by BA08, which predicts the lowest amplitudes of the four considered relations, yields 0.2-s SAs that are two to four times lower than the BB 0.2-s SAs in this area. Even the relations of CY08 and AS08, which predict the highest amplitudes, are exceeded at near-fault hanging-wall locations. On the footwall side of the fault, the BB SAs are in good agreement with BA08. Beyond fault distances of more than 12 km on the hanging-wall side, however, the BB SAs quickly drop below the values predicted by all four NGA models. The simulated SAs are generally within one standard deviation of those predicted by the NGA relations everywhere along the cross section.

Figure 8b shows BB 0.2-s SAs along cross-section P1 for rupture model B'. This example includes the most extreme values produced by our simulations, as rupture model B' yields the largest ground motions of all six scenarios and the cross-section P1 runs through the area with the largest linear BB SAs for this scenario. For fault distances less than

9 km on the hanging-wall side, the linear BB SAs exceed the predictions of all four considered NGA models by more than one standard deviation. All four GMPEs predict the highest SAs on the footwall side of the fault, which is the opposite of the pattern produced by the BB simulations. However, the BB results presented in Figures 6–8 do not take soil nonlinearity into account by any means, the subject of [Nonlinear 1D Simulations](#). (E Fig. S2 of the electronic supplement shows SAs at five different frequencies from 1 to 10 Hz, PGAs, and PGVs for all six scenarios and all three cross sections shown in Fig. 1.)

Nonlinear 1D Simulations

To estimate the impact of nonlinear soil behavior at frequencies above 1 Hz, we carried out fully nonlinear 1D simulations for each site along the three profiles using the methodology previously described. The results of these nonlinear simulations are used to derive nonlinear correction functions that we apply to the entire Salt Lake basin. Figure 9 shows an example of 1D nonlinear simulation for site 100 along profile 1 (P1-100), located 5.3 km west of the fault trace (Fig. 1). The linear BB signal shows spikes with peak accelerations up to $9 \text{ m} \cdot \text{s}^{-2}$ (Fig. 9a). This signal is deconvolved to represent the incoming wave field at depth, and

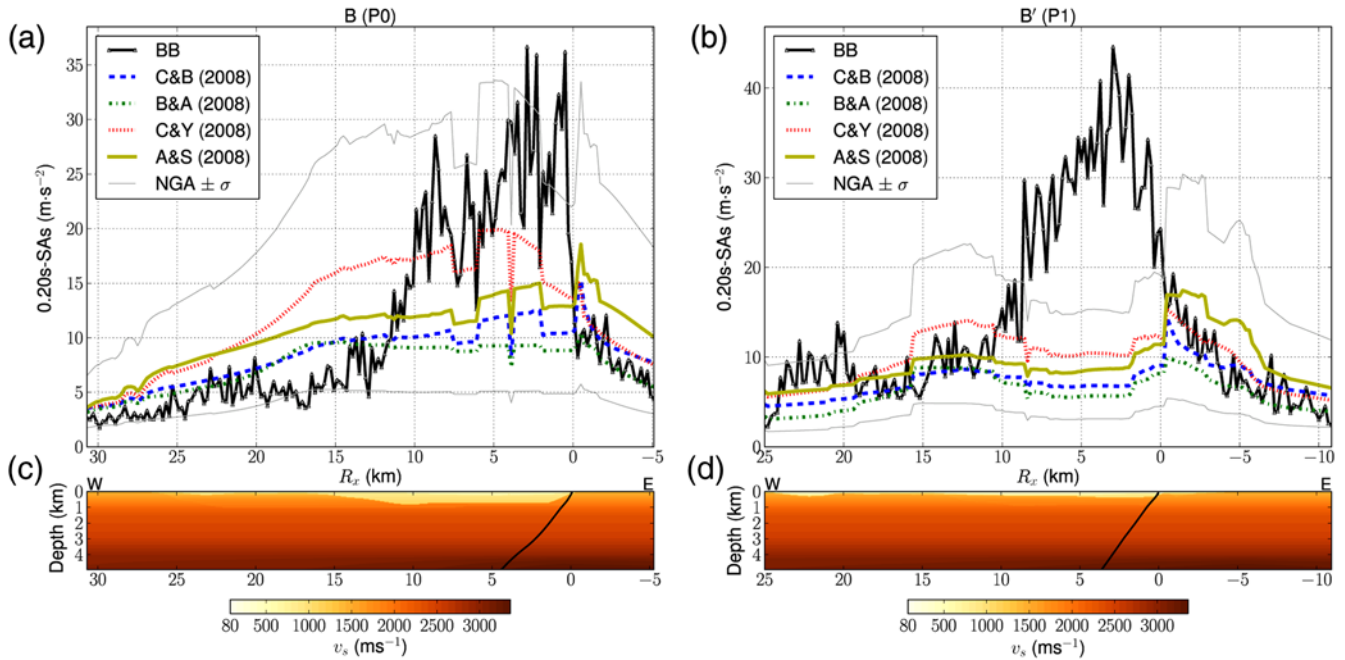


Figure 8. (a, b) 0.2-s SAs predicted by four NGA equations and computed from linear BB synthetics along profile P0 for (a) source model B and along profile P1 for (b) source model B'. See Figure 1 for profile locations. The thin black lines show the largest median plus one standard deviation and the smallest median minus one standard deviation of all four considered NGA Models. (c, d) Cross sections through the WFCVM showing the shear-wave velocity. The black lines indicate the fault. The color version of this figure is available only in the electronic edition.

propagated back to the surface using NOAH. The resulting signal on the surface of the nonlinear layer exhibits lower PGAs of up to $3 \text{ m} \cdot \text{s}^{-2}$.

Spectral accelerations of the nonlinear signal (Fig. 9b) are generally much lower at frequencies above 1 Hz. The original BB signal shows two peaks at 1.6 and 3.7 Hz, with spectral amplitudes of 29 and $29.5 \text{ m} \cdot \text{s}^{-2}$, respectively. Nonlinear site response reduces the amplitudes of the two peaks to 17 and $16 \text{ m} \cdot \text{s}^{-2}$, respectively, and their frequencies are slightly reduced to 1.4 and 2.7 Hz, respectively. This shift of resonance frequencies to lower values is caused by shear modulus degradation due to nonlinear behavior of the soil.

At this site, the soil is allowed to behave nonlinearly in the top 210 m. However, the peak shear strain remains below the reference strain for depths larger than 90 m (Fig. 9c). At depths between 5 and 90 m, the peak shear strain exceeds the reference strain, which indicates that the soil exhibits strong nonlinear behavior. The maximum shear strain and acceleration (Fig. 9d) peak at a depth of 70 m. This peak is probably linked to the local minimum in the shear-wave velocity profile at the same depth (Fig. 9e), which may be trapping the seismic waves. The stress-strain relation (Fig. 9f) is close to linear 100 m below the surface, but becomes increasingly hysteretic with decreasing depth.

Figure 10 shows SAs predicted by the four NGA models for the same profiles as depicted in Figure 8, but compares them with SAs calculated from the fully nonlinear synthetics. For cross-section P0 and rupture model B (Fig. 10a), the nonlinear 0.2-s SAs are generally consistent with the values

predicted by AS08 and CY08 at near-fault ($R_x < 10 \text{ km}$) hanging-wall locations. Spectral accelerations predicted by BA08 and CB08, however, are up to 50% lower than nonlinear 0.2-s SAs on the hanging wall. Compared with the BB 0.2-s SAs, the nonlinear 0.2-s SAs are reduced by up to 45%. On the footwall side and for $R_x > 15 \text{ km}$ on the hanging-wall side, the nonlinear 0.2-s SAs are almost identical to the BB 0.2-s SAs. This observation suggests that the input ground motion at these sites is not sufficient to trigger nonlinear soil behavior for the given soil strength.

We also calculated the site response at every point along the three profiles using the soil models that represent the upper and lower bound of soil nonlinearity, by taking $\gamma_r \mp \sigma$ as the reference strain and $\xi_{\max} \pm \sigma_r$ as the maximum damping ratio. The hatched area in Figure 10a indicates the range of nonlinear 0.2-s SAs obtained from the upper- and lower-bound parameters. The choice of γ_r and ξ_{\max} only affects the ground motion at sites where a significant deamplification due to soil nonlinearity takes place; that is, on the hanging-wall site of the fault for R_x less than about 10 km. Using the lower-bound soil model increases nonlinear 0.2-s SAs by up to 30% at individual sites, while the upper bound model decreases them by up to 25% compared with the reference nonlinear model.

Figure 10b makes the same comparison with nonlinear 0.2-s SAs for cross-section P1 and rupture model B'. Compared with the linear case, 0.2-s nonlinear SAs are reduced by up to 70%, with the largest reduction on the hanging-wall side within a 10-km fault distance. The simulated 0.2-s SAs

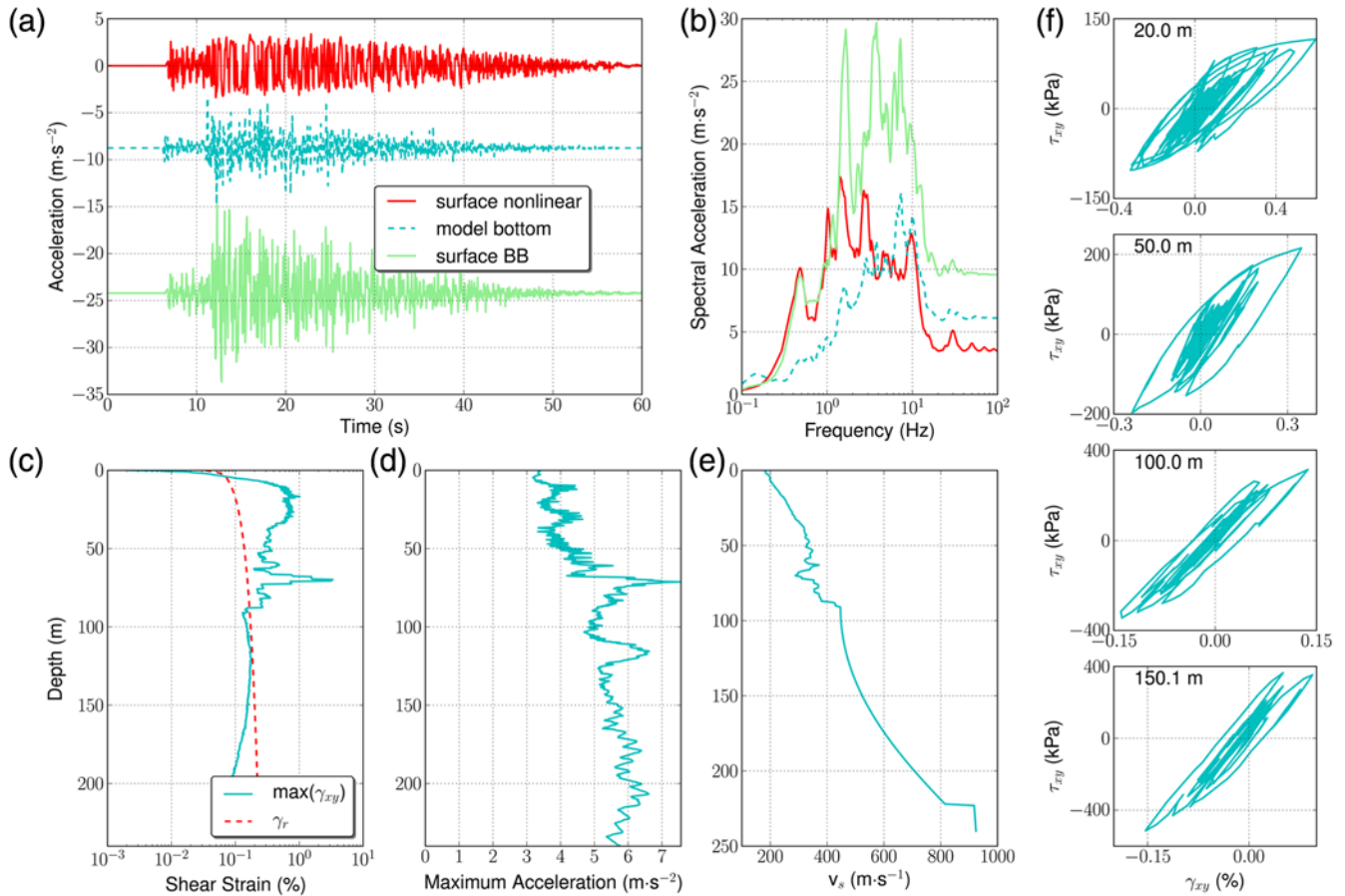


Figure 9. Example of 1D nonlinear simulation for site P1-100 (Fig. 1) showing the east–west component from rupture model B' . (a) Acceleration time series of linear BB ground motion, deconvolved linear BB signal used as input signal, and ground motion on the top of the nonlinear layer. (b) Response spectra of time series depicted in (a). (c) Peak shear strain encountered during the simulation (solid) and reference strain (dashed) as a function of depth. (d) Peak acceleration as a function of depth. (e) Shear-wave velocity profile. (f) Shear stress τ_{xy} versus strain γ_{xy} at different depths. The color version of this figure is available only in the electronic edition.

are in general agreement with the GMPEs. Even when the uncertainty associated with the nonlinear soil parameters is taken into account (hatched area in Fig. 10b), the nonlinear 0.2-s SAs remain mostly inside one standard deviation of the minimum and maximum of the four considered NGA predictions. The largest nonlinear 0.2-s SAs along cross-section P1 occur close to the surface rupture on the footwall side, which is consistent with the pattern predicted by the four GMPEs. Along cross-section P1, all locations on the hanging-wall side belong to site response unit Q01 (Fig. 1), while the footwall side is located on unit Q03 and on rock. This fact suggests that the degree of nonlinearity is controlled by the local site response unit. (E) Fig. S3 in the electronic supplement complements Fig. 10 with nonlinear SA maps at five different frequencies, PGAs, and PGVs for the six scenarios and three cross sections.)

Nonlinear Correction Functions

From the nonlinear simulations carried out along the three cross sections (see the previous discussion), it is clear

that nonlinear effects must be considered throughout the Salt Lake Valley for the *M* 7 Wasatch fault scenarios in order to provide useful ground-motion predictions for structural engineers. However, carrying out fully nonlinear simulations at all sites in the Salt Lake Valley is beyond the scope of this study. Instead, we generate and apply average frequency-dependent correction factors for nonlinear soil effects in the Salt Lake basin.

Toward this goal, we analyzed nonlinear SAs as a function of the corresponding linear SAs for the three different SRUs. To calculate the corresponding linear SAs, we ran 1D simulations with the same input signal and the same velocity profile as in the nonlinear simulations, but defined the material inside the entire soil column as linear. We considered 454 sites located on soil along the three profiles (182 on Q01, 135 on Q02, and 137 on Q03) and six different earthquake scenarios. For each site and each scenario, eight 1D simulations were required. We used one for each horizontal component with four different soil models: mean nonlinear model, upper- and lower-bound nonlinear models, and linear

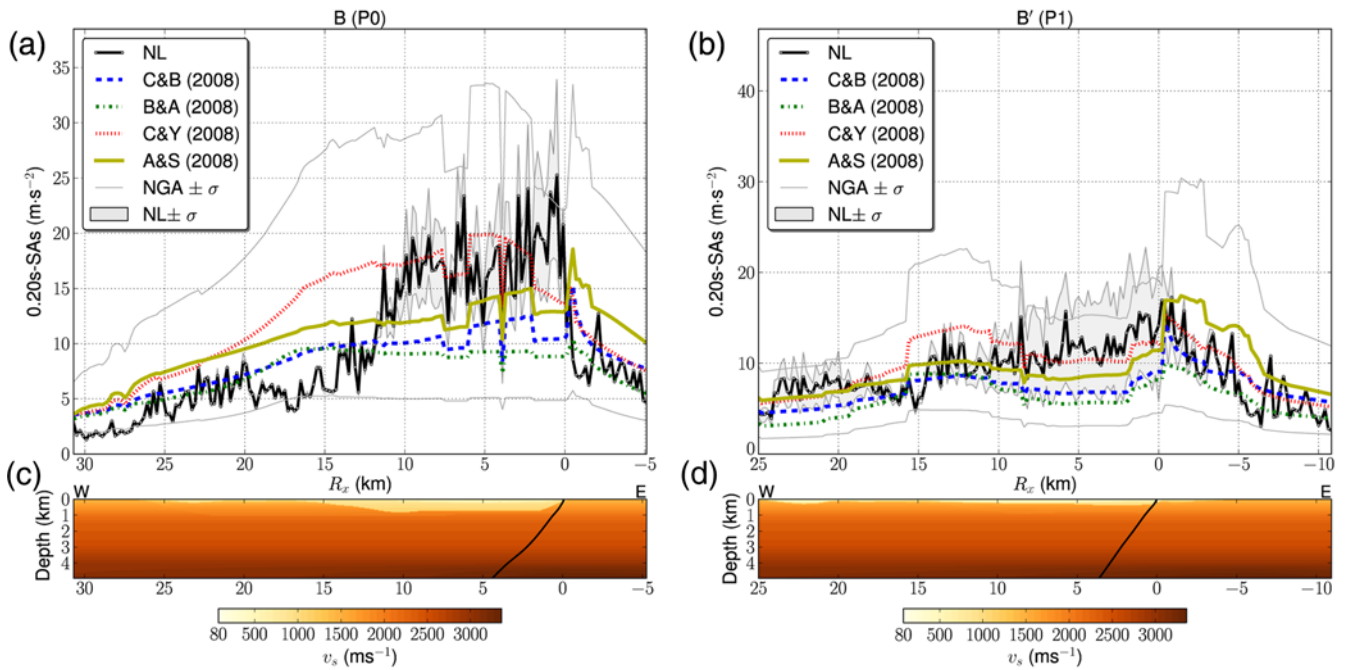


Figure 10. Same as Figure 8, but showing SAs derived from fully nonlinear 1D simulations. The hatched areas depict SAs obtained from the upper- and lower-bound nonlinear models, using $(\gamma_r - \sigma, \xi_{\max} + \sigma_r)$ and $(\gamma_r + \sigma, \xi_{\max} - \sigma_r)$, respectively. The color version of this figure is available only in the electronic edition.

model. Therefore, a total of 21,792 1D simulations were considered to analyze the relations between linear and nonlinear spectral accelerations.

Figure 11a shows nonlinear 0.2-s SAs as a function of linear 0.2-s SAs for all points located on SRU Q01. While the linear time series exhibit 0.2-s SAs up to $50 \text{ m} \cdot \text{s}^{-2}$ ($\sim 5g$), the nonlinear ground motions do not exceed $27 \text{ m} \cdot \text{s}^{-2}$. The linear SAs and nonlinear SAs correlate strongly for small accelerations. The effect of hysteretic damping becomes appreciable for linear SAs above $\sim 5 \text{ m} \cdot \text{s}^{-2}$, and the relation

between linear and nonlinear 0.2-s SAs resembles a sine-shaped curve. However, there is a large scatter in the linear–nonlinear SA data, even for relatively low levels ($< 10 \text{ m} \cdot \text{s}^{-2}$) of linear spectral acceleration.

The linear–nonlinear 0.2-s SAs comparison for SRU Q02 (Fig. 11b) implies a more linear site response and less variability than for Q01. Sites located on Q03 (Fig. 11c) exhibit an even smaller difference between nonlinear and linear 0.2-s SAs. Additionally, the linear ground motion on Q03 tends to be lower than on the other two SRUs, because Q03 is almost

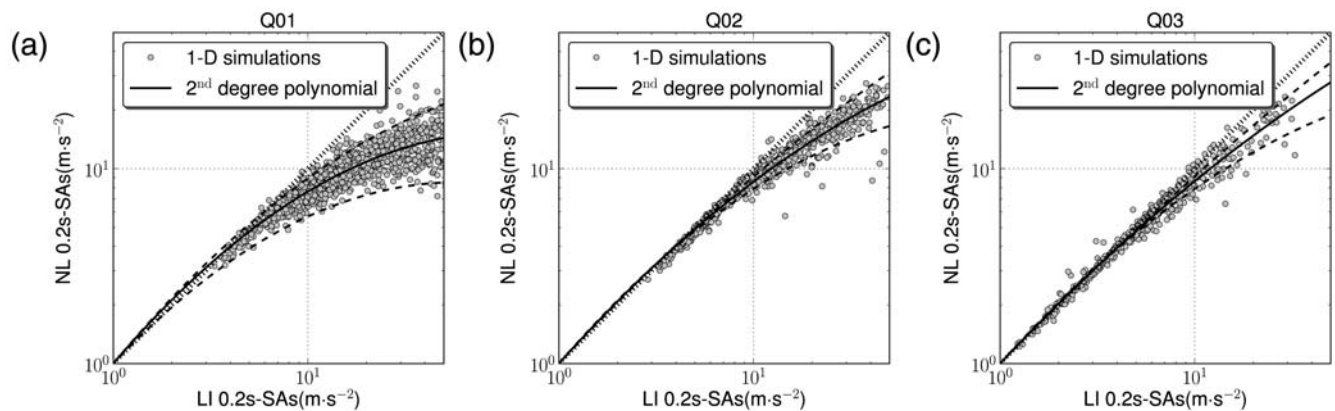


Figure 11. SAs of 0.2 s obtained from nonlinear simulations as a function of corresponding linear values for site response units (a) Q01, (b) Q02, and (c) Q03. Solid lines depict the amplitude- and site-dependent correction functions, obtained by fitting a second-degree polynomial through these data. Dashed lines depict the correction functions derived from nonlinear simulations with the upper- and lower-bound soil models. (Individual data points are shown for the mean soil model only.)

entirely located on the footwall side of the Wasatch fault or at sites located more than 15 km from the surface rupture on the hanging-wall side.

The comparisons between nonlinear and linear 0.2-s SAs presented in Figure 11 suggest that the degree of nonlinearity strongly depends on the local SRU, with the highest deamplification on Q01 and the most linear behavior on Q03. This result is somewhat surprising, as SRU Q01 was assigned the highest plasticity index ($PI = 40$), which implies a higher reference strain and, therefore, supposedly a more linear behavior (e.g., Vucetic and Dobry, 1991). However, there are other factors apart from the reference strain that influence the degree of nonlinearity: the total depth of the nonlinear layer (that is, the depth to the R_1 interface) and the average shear-wave velocity in the soil column.

Figure 12a shows the distribution of the average shear-wave velocity in the top 30 m, V_{S30} , for the three SRUs along the three cross sections inside the computational domain (dashed lines). The V_{S30} values shown in the histograms were computed from the velocity mesh for the FD simulations, where a minimum v_S of $200 \text{ m} \cdot \text{s}^{-1}$ was imposed for computational reasons. V_{S30} is lower than $300 \text{ m} \cdot \text{s}^{-1}$ at most sites classified as Q01, while Q02 is characterized by a V_{S30} of $250\text{--}550 \text{ m} \cdot \text{s}^{-1}$. Sites belonging to Q03 typically have a V_{S30} between 350 and $700 \text{ m} \cdot \text{s}^{-1}$.

According to equation (7), the backbone curve is scaled with the maximum shear stress τ_0 that the material can support in the initial state. τ_0 is proportional to the reference strain γ_r (equation 6) and the low-strain shear modulus

$$G_0 = \rho v_S^2. \quad (16)$$

Because G_0 is proportional to the square of the shear-wave velocity, v_S has a greater impact on the material strength than γ_r . This dependence is illustrated in Figure 3, which shows the theoretical strain-stress relationship according to Masing's rules for two specimens with $\gamma_r = 0.1\%$ and shear-wave velocities of 250 and $300 \text{ m} \cdot \text{s}^{-1}$, respectively. Both materials are subjected to a cyclic shear stress up to $\sim 100 \text{ kPa}$. Figure 3 illustrates how the lower v_S results in a higher energy dissipation, which is proportional to the area of the hysteresis loop (Ishihara, 1996). Note, however, that the area of the hysteresis loop will be reduced in NOAH, because the energy loss is controlled by the maximum damping ratio in equation (9).

Figure 12b shows the distribution of the depth to the R_1 interface for the three SRUs, which corresponds to the total thickness of the nonlinear layer. Similar to the V_{S30} , the depth to R_1 shows a different distribution on the three SRUs. On Q01, R_1 is deeper than 100 m for the majority of the sites, but it is often encountered at depths of less than 50 m on SRU

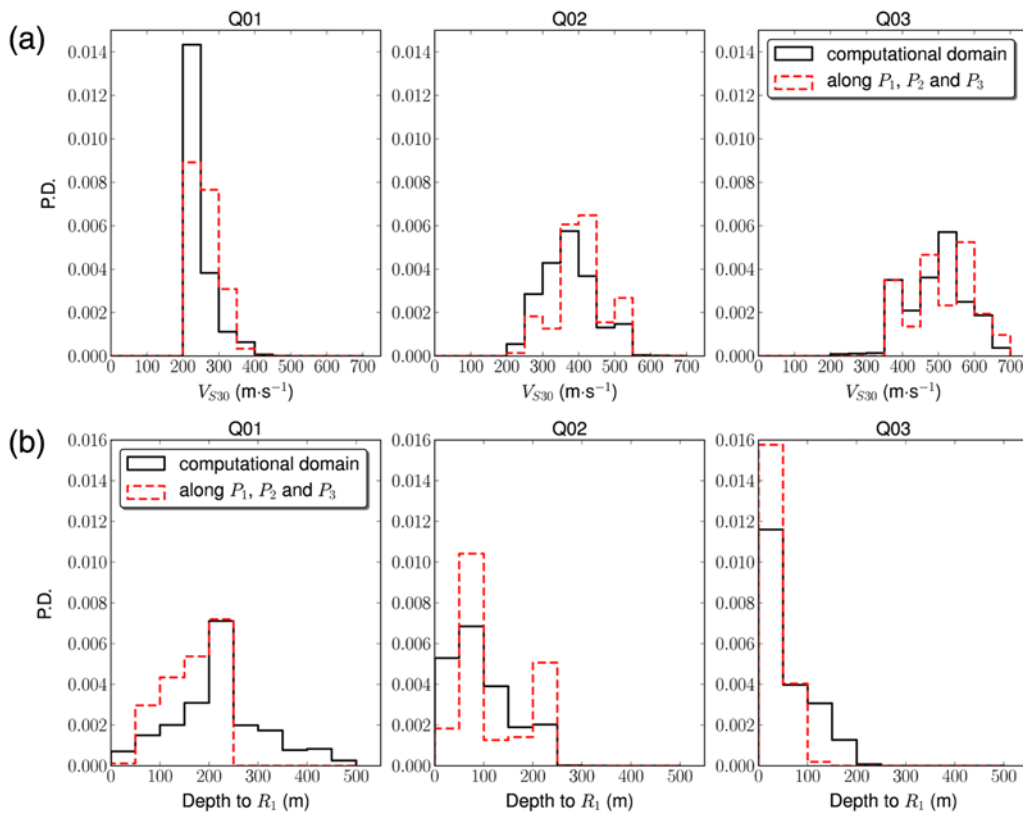


Figure 12. Distributions of (a) average shear-wave velocity in the top 30 m, V_{S30} , and (b) depth to the R_1 interface for the three SRUs. Counts were normalized to form a probability density function. Histograms are shown for the three cross-section lines on Figure 1 (dashed lines) and for the entire computational domain (solid lines). The color version of this figure is available only in the electronic edition.

Q03. Unit Q02 shows an intermediate distribution. A thinner nonlinear layer means that vertically propagating SH waves will encounter hysteretic damping on a smaller fraction of the path, and it is less likely that their amplitude will be reduced significantly by the time they reach the surface. The differences among the three SRUs in the distributions of R_1 depths and V_{S30} values explain why SRU Q03 exhibits the most linear behavior; the strongest nonlinear damping is encountered for SRU Q01, with an intermediate behavior for Q02.

The distributions of V_{S30} and the depths to R_1 along the three cross sections (dashed lines in Fig. 12) are quite representative of the distributions on the entire computational domain (solid gray lines in Fig. 12). We can use this observation to define nonlinear correction functions that depend on the SRU and the amplitude of linear spectral accelerations. To approximate the linear–nonlinear relationship (Fig. 11) a second-degree polynomial was fit to the data after taking the natural logarithm

$$\ln(\text{SA}_{\text{NL}}) = a + b \times \ln(\text{SA}_{\text{LN}}) + c \times \ln^2(\text{SA}_{\text{LN}}), \quad (17)$$

where SA_{NL} represents the nonlinear 0.2-s SAs and SA_{LN} the corresponding linear values. As we expect a strong correlation between linear and nonlinear values for low levels of SA_{NL} , we forced the offset a to zero in the least-squares inversion. This constraint makes the function pass through (1,1) due to the logarithm in equation (17).

The solid line in Figure 11a shows the nonlinear correction function that was fit to the data for Q01, for which we obtained $b = 1.17$ and $c = -0.13$ (see Table S1 in the electronic supplement). We also determined the coefficients b and c for the linear–nonlinear corrections that were obtained from the upper- and lower-bound models of nonlinearity for Q01 (dashed lines in Fig. 11a). The sensitivity of the nonlinear spectral acceleration to the soil parameterization is significant: for linear 0.2-s SAs of $20 \text{ m} \cdot \text{s}^{-2}$, for example, the correction function predicts a nonlinear 0.2-s SA of $11 \text{ m} \cdot \text{s}^{-2}$, while the upper bound nonlinear model yields only $\sim 7 \text{ m} \cdot \text{s}^{-2}$; the lower-bound model predicts $14 \text{ m} \cdot \text{s}^{-2}$. For SRU Q02 and 0.2-s SAs (Fig. 11b), we obtain $b = 1.11$ and $c = -0.08$ with the mean nonlinear model, which reflects the more linear behavior encountered on this SRU. For Q03, the polynomial function deviates only slightly from one, as the least-squares inversion yields $b = 1.06$ and $c = -0.05$.

We determined the coefficients b and c for all of the frequencies considered and PGA. For PGV we allowed the coefficient a to vary, because the slope of the relation between nonlinear and linear PGVs deviates from 1 for linear PGVs below $1 \text{ m} \cdot \text{s}^{-1}$. (Table S1 lists the coefficients b , c , and a , if applicable, for the mean, upper-bound, and lower-bound models, respectively, for all of the SRUs.)

Ground-Motion Maps Corrected for Nonlinearity

We now employ the site- and amplitude-dependent correction functions defined by equation (17) and Table S1 to

correct the linear BB spectral acceleration maps for effects of nonlinear soil behavior (see Table S1 in the electronic supplement). For each node on the $45 \times 60 \text{ km}^2$ grid, the local SRU was determined using a digitized version of the McDonald and Ashland (2008) site response map (Fig. 1). Then we calculated the nonlinear SAs from the corresponding linear SAs using the coefficients b and c appropriate for the given SRU and frequency.

Figure 13a shows 0.2-s SAs for scenario B after application of the nonlinear correction functions (note the different scale compared with the uncorrected BB SA map in Fig. 7a). We obtain 0.2-s SAs of 1.2 to 2.0g on the hanging-wall side in the east-central Salt Lake basin. Compared with the linear BB synthetics, the nonlinear 0.2-s SAs were reduced from $> 2.25g$ to $\sim 1.2g$ in the Murray area. The largest patch of high ($> 1.6g$) 0.2-s SAs after application of the correction factors is located south of the Cottonwood Heights area on SRU Q02.

For scenario B' (Fig. 13b), 0.2-s SAs are generally between 1.2 and 1.6g in most near-fault hanging-wall areas, including the central Salt Lake City area, which is a significant reduction compared with the $> 2.25g$ from the uncorrected map (Fig. 7b). However, there are small patches with 0.2-s SAs above 1.6g, including one in a part of downtown Salt Lake City, which is classified as Q02 in the McDonald and Ashland SRU map (Fig. 1). Spectral accelerations of 0.2 s also exceed 1.2g at locations on the footwall side, which suggests that nonlinear soil behavior reduces the differences between the footwall and hanging-wall side at higher frequencies. (The electronic supplement contains maps for each of the six scenarios with SA at other frequencies, PGAs, and PGVs corrected for nonlinear soil behavior. See Fig. S4 in the supplement.)

We calculated the geometric mean of SAs, PGA, and PGV from the ensemble of six scenarios after applying the site- and amplitude-dependent nonlinear corrections. Figure 14a shows mean spectral accelerations at a period of 1 s. Spectral accelerations of 1 s exceed 0.5g in a region 5–10 km wide on most of the hanging wall, with values of 0.75–1.0g in a narrower zone 3–5 km wide that includes downtown Salt Lake City. On the footwall side, 1-s SAs are between 0.25 and 0.75g on the sediments in the central Salt Lake basin and below 0.5g on rock. The 1-s SAs reported by Solomon *et al.* (2004) on the hanging wall within 5–10 km of the fault trace are comparable to our values in the central and northern Salt Lake basin, 0.7–1.1g, but significantly higher than our values in the southern Salt Lake basin, up to 1.3–1.5g. Perhaps more significantly, Solomon *et al.* (2004) obtained higher average 1-s SAs for the sediments on the footwall side (up to 1.1–1.5g) than on the hanging-wall side in the central Salt Lake basin area, in contrast to our results (Fig. 14a).

Our simulated mean 0.2-s SAs (Fig. 14b) generally exceed 1 g on the hanging-wall side and on sediments near the fault on the footwall side in the central Salt Lake basin. Average PGAs from the ensemble of the six scenarios

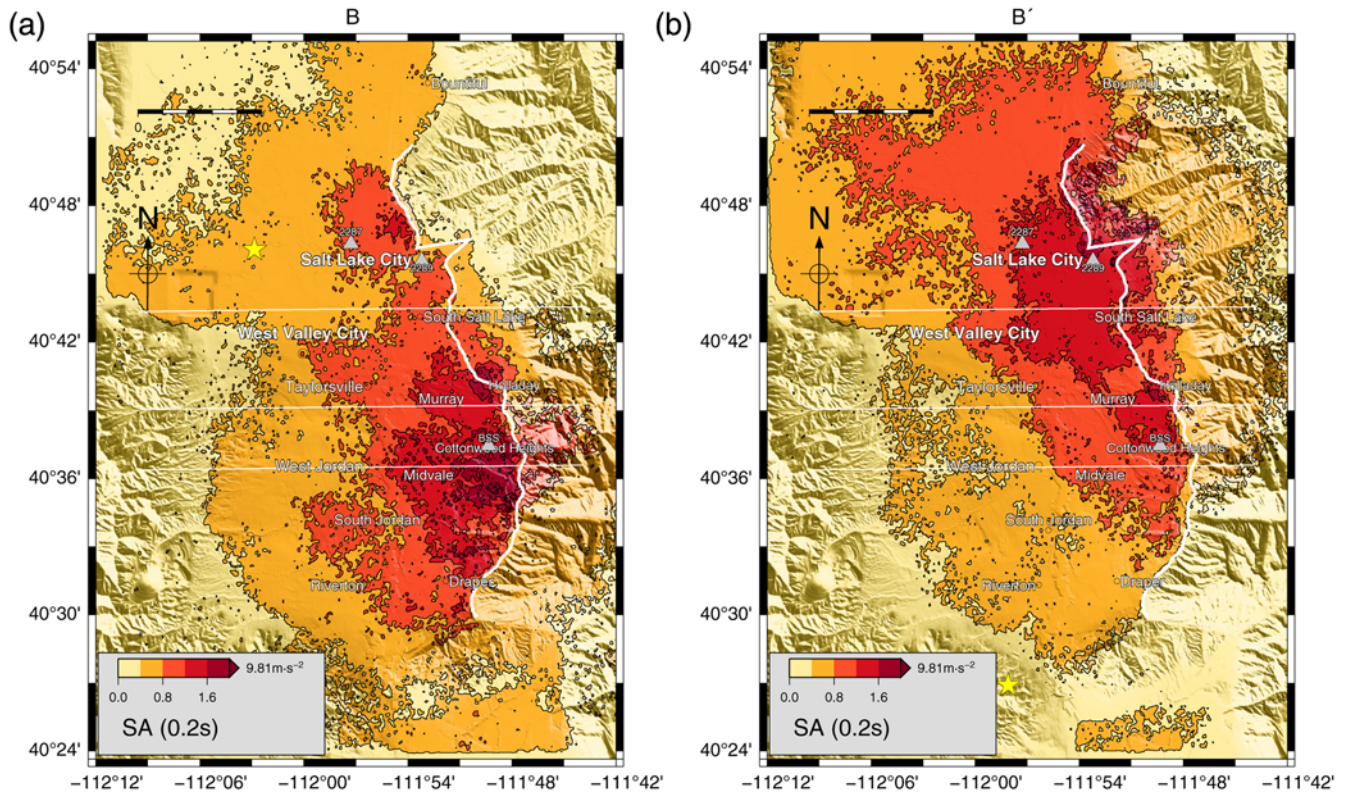


Figure 13. Maps of orientation-independent spectral accelerations, corrected for nonlinear soil behavior. (a) 0.2-s SAs for rupture model B. (b) 0.2-s SAs for rupture model B'. The color version of this figure is available only in the electronic edition.

(Fig. 14c) show a spatial distribution that is very similar to the 0.2-s SAs. Peak ground accelerations average $\sim 0.45g$ at near-fault locations on the sediments and exceed $0.6g$ in the previously identified patches on the hanging-wall side. Compared with the predicted mean of 0.2-s SAs and PGAs of Solomon *et al.* (2004), our values are generally lower and show a stronger correlation with distance to the surface rupture and a weaker correlation with the SRUs.

Both 0.2-s SAs and PGAs show little contrast between the hanging-wall side and footwall side in the central Salt Lake basin, where sediments are found on both sides of the fault. Average SA maps at 2 s and 3 s, however, show larger values on the hanging wall in most places (Roten *et al.*, 2011), including sites in the central Salt Lake basin. This observation, as well as the comparison between Figures 7 and 13, suggests that soil nonlinearity helps to eliminate the

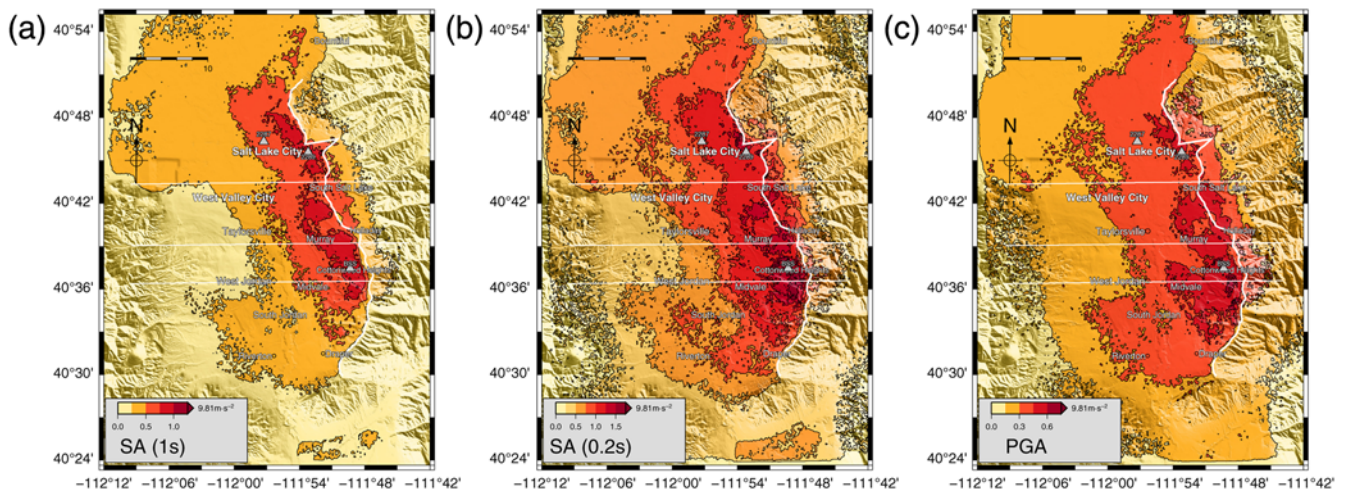


Figure 14. (a) Average 1-s SAs, (b) 0.2-s SAs, and (c) PGAs from the six scenarios after application of nonlinear correction functions. The color version of this figure is available only in the electronic edition.

differences in amplification between the deep, soft sediments on the hanging-wall side and the shallow, stiff sediments on the footwall side at higher frequencies: A low V_{S30} and deep R_1 interface, as found in SRU Q01 (Fig. 12), favor long-period amplification but also cause more HF deamplification due to nonlinearity. Conversely, sites characterized by a shallow R_1 interface and higher V_{S30} (Q03) will not experience much amplification at longer periods, but are less prone to hysteretic damping at higher frequencies.

Comparison with GMPEs

We now perform a systematic comparison between the simulated 0.2-s SAs and 0.1-s SAs and the values predicted by the four GMPEs considered earlier. We calculated the different source distances and the required site characterization parameters for each Salt Lake basin point on the computational grid. Source distance parameters were computed from the 3D fault model that was used for the 3D FD simulations. Site characterization parameters such as V_{S30} , the depth to $V_S \geq 2.5 \text{ km} \cdot \text{s}^{-1}$ (required by AS08), and the depth to $V_S \geq 1.0 \text{ km} \cdot \text{s}^{-1}$ (required by CY08), were extracted from the WFCVM. Using these parameters, we computed spectral accelerations, PGAs, and PGVs at each point on the 200 m by 200 m grid with the four GMPEs.

For each scenario and each location j , we evaluated the residual r_j between the simulated SA (SA_{sim}) and the value predicted by the GMPE (SA_{emp}), and normalized it with the standard deviation of the GMPE (σ_{emp}):

$$r_j = \frac{\ln(SA_{\text{sim},j}) - \ln(SA_{\text{emp},j})}{\sigma_{\text{emp},j}}. \quad (18)$$

We binned the residuals into 50 rupture-distance (R_{Rup}) categories spaced logarithmically between 1 and 22 km. We evaluated the bias by averaging over all the residuals r_k inside a distance bin:

$$B_k = \frac{1}{N_k} \sum_1^{N_k} r_k, \quad (19)$$

where N_k denotes the number of observations within the distance range. Thus, a positive bias indicates that the simulations overpredict the value returned by the GMPE. We evaluated the bias for the SAs obtained from the BB synthetics on soil sites both before and after application of the nonlinear correction functions.

Figure 15 shows the bias in 0.2-s SAs and 0.1-s SAs as a function of rupture distance R_{Rup} for the GMPEs of BA08, CB08, CY08, and AS08. For 0.2-s SAs and BA08, both the linear and nonlinear biases are close to zero at rupture distances larger than 7 km. For $R_x < 5$ km, however, the bias of the linear results is close to 1σ . After application of the nonlinear correction function, this bias is reduced to less than 0.5σ . The same effect can be observed for the relation of

CB08. This result indicates that the correction for nonlinear soil behavior makes the simulated ground-motion maps more consistent with these two GMPEs.

Because CY08 and AS08 tend to predict higher ground-motion values, we obtain different patterns for the bias for these two relations. At rupture distances less than 5 km, the bias is between 0 and 0.9σ in the linear case and between -0.25σ and -0.75σ in the nonlinear case. For rupture distances larger than 7 km, the bias is between -0.5σ and -1σ in the linear case, with larger negative values after the nonlinear correction factors are applied.

The comparison for 0.1-s SAs shows a very similar pattern. Without the nonlinear correction, the simulated values are above all the GMPEs at small rupture distances ($R_x < 5$ km), even by more than one standard deviation in the case of BA08 and CB08. The nonlinear corrections make the simulated 0.1-s SAs more consistent with the four GMPEs at $R_x < 5$ km, yielding a positive bias for BA08 and CB08, a negative bias for CY08, and a bias that averages near zero for AS08.

While the systematic comparison shows that the simulated 0.2-s SAs and 0.1-s SAs are, on average, in agreement with the four GMPEs, the spatial distribution of simulated SAs is in strong contrast with the pattern predicted by the GMPEs. Figure 16a is a map of 0.2-s SAs predicted by BA08. As this relation uses only the Joyner–Boore distance to the fault, R_{JB} , areas within $R_{\text{JB}} = 0$ are characterized by similar spectral accelerations regardless of the distance to the surface rupture. For example, the West Jordan area located ~ 15 km from the rupture is assigned a 0.2-s SA value between 0.75 and 1.0g by BA08. The same range of 0.2-s SAs is predicted for the area around the Holladay stepover in the immediate vicinity of the rupture. This pattern is very different from the average of the ensemble of the six simulations (Fig. 14b) that predicts the highest ground motion on the hanging-wall side to be near the surface rupture: we obtain average 0.2-s SAs above 1.25g near the Holladay stepover and only 0.25–0.75g in the West Jordan area. Even though the other three GMPEs use additional source distance measurements, they share a strong dependence on R_{JB} via factors that account for higher ground motions on hanging-wall sites compared with footwall sites (Ⓔ see Fig. S6 in the electronic supplement). CY08 also predict similar 0.2-s SAs at some near-fault locations and hanging-wall locations 15 km from the surface rupture (Fig. 16b). Another striking difference between the mean of the ensemble (Fig. 14b) and the relations by BA08 (Fig. 16a), CY08 (Fig. 16b), and AS08 (Ⓔ see Fig. S6 in the electronic supplement) is that the latter three generally predict higher 0.2-s SAs on the footwall side than on the hanging-wall side in the central part of the Salt Lake basin. This pattern is also found in the maps by [Silva, Gregor, et al. \(2002\)](#) and [Solomon et al. \(2004\)](#).

Because the amplitude of the HF component in the BB synthetics depends on the level of the LF component, maps with SAs at higher frequencies resemble those for longer periods (Fig. 14). Maps with SAs predicted by GMPEs, on

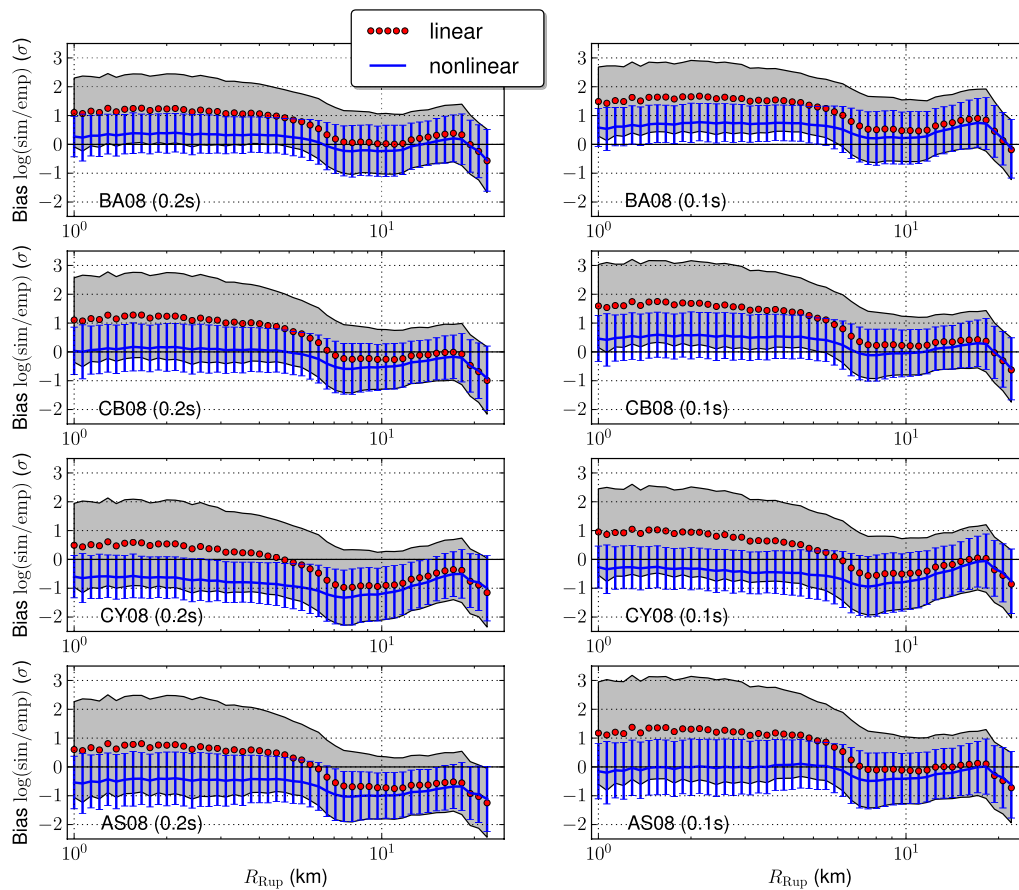


Figure 15. Bias of simulated 0.2-s SA and 0.1-s SAs on Salt Lake basin sediments compared with four GMPEs (equation 19). Shaded areas show standard deviations of the residuals from our linear results; error bars show standard deviations of the nonlinear residuals. The color version of this figure is available only in the electronic edition.

the other hand, exhibit a different spatial distribution depending on the analyzed frequency (see Fig. S6). Longer-period (2 s, 3 s) SAs are especially high on the hanging-wall side within ~ 10 km of the surface rupture, and this pattern is also reproduced by the LF FD simulations. Shorter-period (0.1 s–0.5 s) SAs predicted by the GMPEs are characterized by a wider distribution of large values extending from the western Salt Lake basin well into the footwall. This behavior is not well reproduced by the BB synthetics. Possible causes for this discrepancy are discussed in [Uncertainty of Computed Nonlinear BB Ground Motions for the Salt Lake Valley](#).

Another observation is that the GMPEs generally predict lower 0.2-s SAs for sites with $V_{S30} < 300 \text{ m} \cdot \text{s}^{-1}$ than for sites with higher V_{S30} , obviously by incorporating nonlinear soil effects in their site amplification terms. As a result, maps with 0.2-s SA predicted by the GMPEs feature the highest values on sediments with V_{S30} above $300 \text{ m} \cdot \text{s}^{-1}$ (Q02 and Q03) and $R_{JB} = 0$ (compare, for example, Figs. 1 and 16). The wedge-shaped region extending from downtown Salt Lake City to Murray is classified as Q01 (Fig. 1) and characterized by $V_{S30} < 300 \text{ m} \cdot \text{s}^{-1}$ (Fig. 12a), which is expressed in the generally low 0.2-s SAs that BA08 and CB08 predict for this area. Our simulated BB synthetics cor-

rected for nonlinear soil behavior, on the other hand, do not show this drastic deamplification for 0.2-s SAs at Q01 sites. However, nonlinear soil effects reduce the difference between sites located on Q01 and Q02. The reason for the lack of deamplification on Q01 could be the rather high reference strain that we assigned to sites belonging to Q01, which reflects the high clay component of the Bonneville soils and the results of laboratory tests on soil samples (Bay and Sasanakul, 2005). The GMPEs, on the other hand, are only estimating soil nonlinearity as a function of the V_{S30} , without taking into account specific soil types.

Uncertainty of Computed Nonlinear BB Ground Motions for the Salt Lake Valley

In this section we discuss the limitations and major sources of uncertainty for our $M 7$ scenario earthquake ground motions in the Salt Lake Valley.

Computation of (Linear) BB Ground Motions

Published hybrid BB generation methods differ in the details of merging the LF and HF portions of the synthetics, as well as in the dependency of the HF part on the local

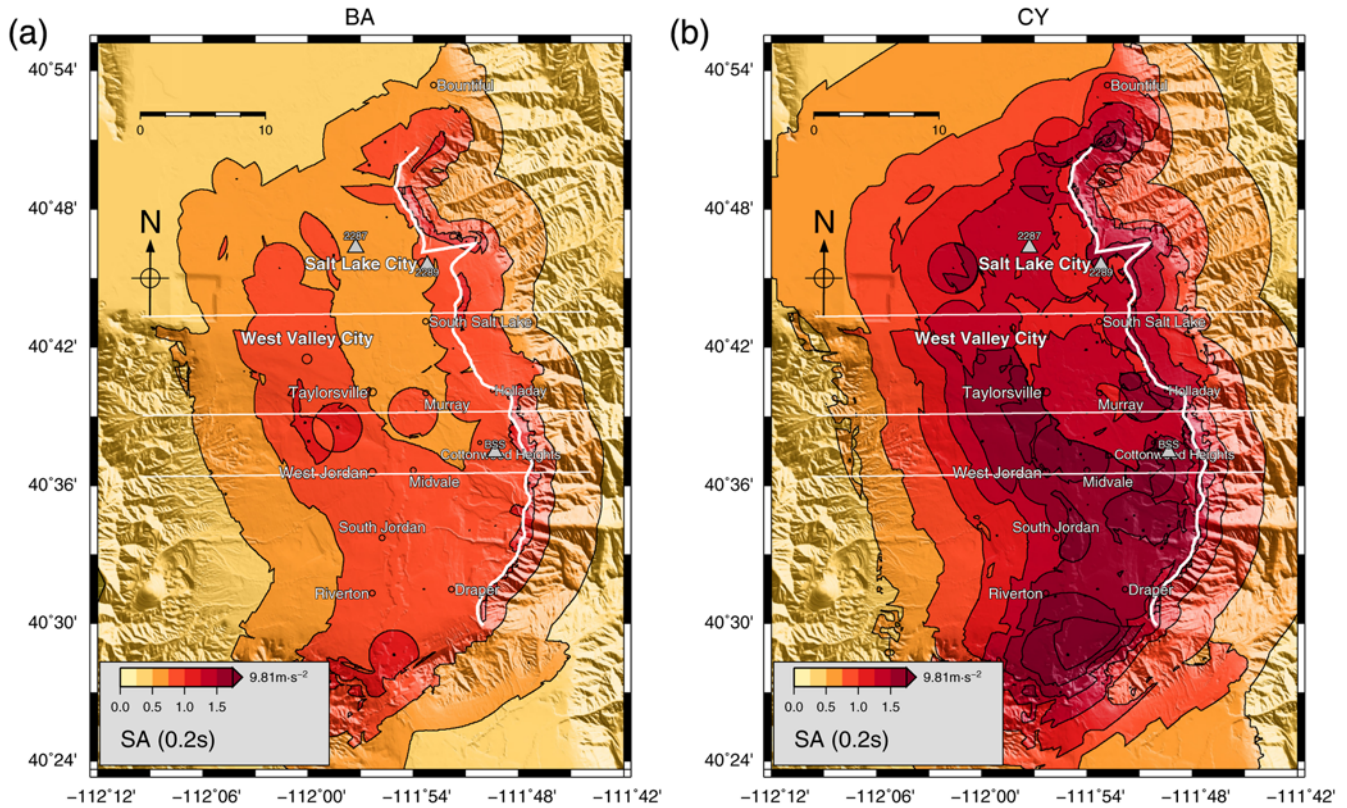


Figure 16. 0.2-s SAs predicted by the GMPE of (a) BA08 and (b) CY08. The color version of this figure is available only in the electronic edition.

impedance structure. For example, the method by [Graves and Pitarka \(2010\)](#) incorporates effects of the velocity structure into the HF part of the spectrum, which is otherwise independent of the LF spectral level. On the other hand, the HF scatterograms computed by the method of [Mai et al. \(2010\)](#) are scaled with the amplitude of the LF spectra at the matching frequency (0.9 ± 0.1 Hz), in part to minimize numerical artifacts at the merging frequency for the LF and HF portions, but also to transfer impedance effects from the LFs into the HF. This dependency between the amplitudes of the LF and HF components in the BB synthetics causes, to some extent, the distributions of SAs at higher frequencies to resemble those for longer periods (Fig. 14). Maps with SAs predicted by GMPEs generally exhibit a different spatial distribution depending on the analyzed frequency (see Fig. S6 in the electronic supplement) as noted in [Nonlinear 1D Simulations](#). Future validation exercises for normal-faulting events should focus on resolving this issue.

Computation of Nonlinear Ground Motions

The assumptions involved in simulating nonlinear soil behavior represent some limitations to this study. A first source of uncertainty concerns the nonlinear soil parameters γ_r and ξ_{\max} . While the empirical relations we used to estimate these parameters were modified based on laboratory tests of Bonneville clay samples, only one of the sampling

locations was inside the area considered for this study. No laboratory measurements were performed on soil samples representing SRUs Q02 and Q03, so the lower reference strains assigned to these units are based solely on the relationship by [Darendeli \(2001\)](#). To analyze the sensitivity of our results to the parameter selection, we included soil models that represent 1σ limits of soil nonlinearity. Results obtained with the lower-bound nonlinear model (Fig. 10) suggest that nonlinearity has a significant impact at near-fault hanging-wall sites even for a more conservative choice of reference strain. Furthermore, we have demonstrated that the degree of nonlinear damping is also largely controlled by V_{S30} and the depth to the R_1 interface, which are reasonably well-constrained parameters ([Magistrale et al., 2008](#)).

The simplicity of the soil model, which neglects dilatancy, constitutes a further limitation. Observations of spiky waveforms, for example, during the 1987 Superstition Hills earthquake ([Holzer et al., 1989](#); [Zeghal and Elgamal, 1994](#)), the 1995 Hyogo-ken Nanbu earthquake ([Kamae et al., 1998](#)), and the 1993 Kushiro-Oki earthquake ([Iai et al., 1995](#)), support the idea that soft soils partly recover their shear strength under cyclic loads due to their dilatant nature ([Bonilla et al., 2005](#)). During this short recovery phase the soil regains its capability to transmit the incoming seismic energy to the surface, leading to characteristic cusped waveforms that represent large amplifications. Modeling dilatancy with NOAH requires five additional parameters that need to be

calibrated from stress-controlled laboratory experiments (e.g., Iai *et al.*, 1990a; Bonilla, 2001; Roten *et al.*, 2009). To our knowledge, no such measurements have been performed on soil samples from the Salt Lake region, which led us to ignore dilatancy in our nonlinear simulations. Including dilatancy may result in higher spectral accelerations, especially on the hanging-wall side.

An additional uncertainty arises from correcting the SAs for nonlinearity with the empirically derived correction functions, as the relations between linear and nonlinear SAs show a lot of variability. Calculating the 1D nonlinear site response for each location on the computational grid individually would eliminate the need for this approximation. This goal could be achieved by performance optimizations in NOAH and by embedding the code into a parallel program that runs on 100 s of central processing unit cores, which would allow the computation of the 1D nonlinear response for the whole Salt Lake basin within a practical time frame.

Finally, the assumption that the site response is adequately represented by vertical wave propagation in a 1D model is likely to represent the largest limitation. In geotechnical engineering it is generally accepted that the major part of ground-shaking is related to upward propagation of body waves (e.g., Ishihara, 1996). This assumption is often justified with the bending of seismic rays toward the Earth's surface, because seismic velocities increase with depth in a typical geological setting. However, Bard and Bouchon (1980) demonstrated that Love waves generated at a basin edge may have much larger amplitudes than the direct incident signal, even in the case of vertical incidence. Such basin-diffracted waves have been identified in many weak-motion records (e.g., Field, 1996; Hartzell *et al.*, 2003; Roten *et al.*, 2008). The physics of surface wave propagation in nonlinear media is an ongoing field of research, and numerical codes are under development that will allow the treatment of wave propagation in nonlinear materials in 2D (e.g., Bonilla *et al.*, 2006) or 3D (e.g., Taborda and Bielak, 2008).

Conclusions

We apply the hybrid BB method of Mai *et al.* (2010), including a finite-fault approximation developed by Mena *et al.* (2010), to add a HF (1–10 Hz) component to the LF (0–10 Hz) FD synthetics produced for an *M* 7.0 earthquake on the WFSLC (Roten *et al.*, 2011). Comparisons with the ground motions predicted by four recent NGA relations show that 0.1-s SAs and 0.2-s SAs derived from the linear BB synthetics often exceed empirical SA estimates by more than one standard deviation at near-fault hanging-wall locations. Because SAs at 2 s and 3 s agree well with empirical values (Roten *et al.*, 2011), we infer that the mismatch at higher frequencies is caused by nonlinear soil behavior, which was neglected in the BB generation methodology.

Using the nonlinear 1D propagator NOAH we calculate the site response in a yielding soil at 454 sites arranged along three east–west cross sections. The input signal for these

simulations is obtained by deconvolving BB synthetics at the free surface to a subsurface location at a depth of 240 m under the assumption of vertical incidence. We use a simple soil model that only requires the reference strain γ_r and maximum damping ratio ξ_{\max} as additional parameters, which we estimate from empirical relationships (Darendeli, 2001) that were modified based on laboratory tests on Bonneville clay samples (Bay and Sasanakul, 2005). Spectral accelerations of the resulting nonlinear 0–10 Hz synthetics are in agreement with GMPE predictions within approximately 1σ , including sites at near-fault hanging-wall locations. We find the largest deamplification due to nonlinear damping on site response unit Q01, which has a lower V_{S30} ($< 300 \text{ m} \cdot \text{s}^{-1}$) and a thicker unconsolidated sediment layer than units Q02 and Q03. This result suggests that the degree of nonlinearity is largely controlled by the depth to the R_1 interface and the V_{S30} , and only to a lesser extent by the choice of γ_r and ξ_{\max} .

We establish amplitude-dependent relations between SAs derived from BB synthetics and SAs resulting from the fully nonlinear 1D simulations. Coefficients for these relations are calibrated for each considered frequency and each of the three site response units. We apply these relations to correct our BB SA maps for nonlinear soil behavior. We find that, after taking soil nonlinearity into account, the largest 1-s SAs still occur on the hanging-wall side of the fault, where the average values exceed $0.75g$. Average 0.2-s SAs are generally above $1g$ within a few kilometers of the fault on the hanging-wall and on the footwall sediments in the central Salt Lake basin. In a few isolated areas, 0.2-s SAs exceed $1.25g$, especially on Q02 in the southern part of the Salt Lake basin. Average PGAs range from 0.45 to $> 0.6g$.

Compared with ground-motion maps generated in previous studies (Wong, Silva, Gregor, *et al.*, 2002; Solomon *et al.*, 2004), our ground-motion values are lower and have a different spatial pattern. The differences between our ground-motion results and those obtained by Wong, Silva, Gregor, *et al.* (2002) and Solomon *et al.* (2004) are likely caused by differences in the simulation methods. Spectral accelerations at 0.2 s and 0.1 s corrected for nonlinear soil behavior compare favorably with values predicted by four GMPEs, including areas at close distances ($< 5 \text{ km}$) from the rupture. However, on our maps the ground motions decrease more rapidly with distance from the surface rupture. Further comparisons against strong motion data are required to validate the simulated ground motions in the future.

Data and Resources

The Wasatch Front Community Velocity Model (WFCVM) is available from the Utah Geological Survey (http://geology.utah.gov/ghp/consultants/geophysical_data/cvm.htm, last accessed May 2012). The nonlinear 1D code NOAH (Bonilla *et al.*, 2005) and the BB toolbox (Mai *et al.*, 2010; Mena *et al.*, 2010) are available from their authors upon request. Maps presented in this text were made using the Generic Mapping Tools version 4.5.0 (<http://www>

.soest.hawaii.edu/gmt, last accessed May 2012) by Wessel and Smith, 1998. Two-dimensional plots were created with the Matplotlib graphics package (<http://matplotlib.sourceforge.net>, last accessed May 2012) for Python (Hunter, 2007). We used the OPENSHA attenuation relationship plotter (<http://www.opensha.org>, last accessed May 2012) and the MatLab™scripts from the Baker research group (<http://www.stanford.edu/~bakerjw/attenuation.html>, last accessed May 2012) to generate attenuation curves.

Acknowledgments

The authors are grateful to Martin Mai and an anonymous reviewer for their valuable comments that helped to improve the paper. We wish to thank Luis Fabián Bonilla for providing the NOAH code and for his support in adapting the soil model. We are grateful to Martin Mai, Banu Mena Cabrera, and Walter Imperatori for making the BB toolbox available and for their helpful advice. The authors thank James A. Bay for his advice in nonlinear parameter selection. This research was supported by a fellowship for prospective researchers (to D.R.) from the Swiss National Science Foundation (PBEZ22-117264) and by the U.S. Geological Survey, Department of the Interior, under USGS award numbers 06HQGR0205, 06HQGR0206, and G11AP20055.

References

- Abrahamson, N., and W. Silva (2008). Summary of the Abrahamson & Silva NGA ground-motion relations, *Earthquake Spectra* **24**, no. 1, 67–97.
- Bard, P.-Y., and M. Bouchon (1980). The seismic response of sediment-filled valleys. Part 1. The case of incident *SH* waves, *Bull. Seismol. Soc. Am.* **70**, no. 4, 1263–1286.
- Bay, J. A., and I. Sasanakul (2005). Measurement of nonlinear dynamic properties of Bonneville silty-clays, *Final Tech. Rept.*, Dept. of Civil and Environmental Engineering, Utah State University, Logan, Utah, Award 04HQGR0055.
- Black, B. D., W. R. Lund, and B. H. Mayes (1995). Large earthquakes on the Salt Lake City segment of the Wasatch fault zone—summary of new information from the South Fork Dry Creek site, Salt Lake County, Utah, in *Environmental and Engineering Geology of the Wasatch Front Region: 1995 Symposium and Field Conference*, W. R. Lund (Editor), Utah Geol. Assoc., Salt Lake City, Utah, 22–23 September 1995, 11–30.
- Bonilla, L. F. (2000). Computation of linear and nonlinear site response for near field ground motion, *Ph.D. Thesis*, University of California, Santa Barbara, California.
- Bonilla, L. F. (2001). *NOAH: Users Manual*, Institute for Crustal Studies, University of California, Santa Barbara, California.
- Bonilla, L. F., R. J. Archuleta, and D. Lavallée (2005). Hysteretic and dilatant behavior of cohesionless soils and their effects on nonlinear site response: Field data observations and modeling, *Bull. Seismol. Soc. Am.* **95**, no. 6, 2373–2395.
- Bonilla, L. F., D. Lavallée, and R. J. Archuleta (1998). Nonlinear site response: Laboratory modeling as a constraint for modeling accelerograms, K. Irikura, K. Kudo, H. Okada, T. Sasatani, and A. A. Balkema (Editors), *Proc. of the 2nd International Symposium on the Effects of Surface Geology on Seismic Motion*, Yokohama, Japan, 1–3 December 1998, vol. 2, 793–800.
- Bonilla, L. F., P.-C. Luis, and S. Nielsen (2006). 1D and 2D linear and nonlinear site response in the Grenoble area, in *3rd International Symposium on the Effects of Surface Geology on Seismic Motion*, Grenoble, France, 30 August–1 September 2006.
- Boore, D. M., and G. M. Atkinson (2008). Ground-motion prediction equations for the average horizontal component of PGA, PGV, and 5%-damped PSA at spectral periods between 0.01 s and 10.0 s, *Earthquake Spectra* **24**, no. 1, 99–138.
- Boore, D. M., J. Watson-Lamprey, and N. A. Abrahamson (2006). Orientation-independent measures of ground motion, *Bull. Seismol. Soc. Am.* **96**, no. 4A, 1502–1511.
- Borcherdt, R. D. (1994). Estimates of site-dependent response spectra for design (methodology and justification), *Earthquake Spectra* **10**, 617–653.
- Brocher, T. (2006). Key elements of regional seismic velocity models for ground motion simulations, in *Proc. of Int. Workshop on Long-Period Ground Motion Simulations and Velocity Structures*, Tokyo, Japan, 14–15 November 2006.
- Bruhn, R. L., P. R. Gibling, W. Houghton, and W. T. Parry (1992). Structure of the Salt Lake segment, Wasatch normal fault zone: Implications for rupture propagation during normal faulting, in *Assessment of Regional Earthquake Hazards and Risk Along the Wasatch Front, Utah, U.S. Geol. Surv. Prof. Pap. 1500-A-J*, H1–H25.
- Campbell, K. W., and Y. Bozorgnia (2008). NGA ground motion model for the geometric mean horizontal component of PGA, PGV, PGD and 5% damped linear elastic response spectra for periods ranging from 0.01 to 10 s, *Earthquake Spectra* **24**, no. 1, 139–171.
- Chiou, B. S.-J., and R. R. Youngs (2008). An NGA model for the average horizontal component of peak ground motion and response spectra, *Earthquake Spectra* **24**, no. 1, 173–215.
- Cui, Y., K. B. Olsen, K. Lee, J. Zhou, P. Small, D. Roten, G. Ely, D. K. Panda, A. Chourasia, J. Levesque, S. M. Day, and P. Maechling (2010). Scalable earthquake simulation on petascale supercomputers, in *Proc. of SC10*, New Orleans, Louisiana, 13–19 November 2010.
- Dalguer, L. A., and S. M. Day (2007). Staggered-grid split-node method for spontaneous rupture simulation, *J. Geophys. Res.* **112**, B02302, 15 pp.
- Darendeli, Mehmet B. (2001). Development of a new family of normalized modulus reduction and material damping curves, *Ph.D. Thesis*, University of Texas, Austin, Texas.
- Day, S. M. (1998). Efficient simulation of constant *Q* using coarse-grained memory variables, *Bull. Seismol. Soc. Am.* **88**, no. 4, 1051–1062.
- Dreger, D., E. Tinti, and A. Cirella (2007). Slip velocity function parameterization for broadband ground motion simulation, *Seismol. Res. Lett.* **78**, no. 2, 308.
- Field, E. H. (1996). Spectral amplification in a sediment-filled valley exhibiting clear basin-edge-induced waves, *Bull. Seismol. Soc. Am.* **86**, 991–1005.
- Graves, R. W., and A. Pitarka (2010). Broadband ground-motion simulation using a hybrid approach, *Bull. Seismol. Soc. Am.* **100**, no. 5A, 2095–2123.
- Hardin, B. O., and V. P. Drnevich (1972). Shear modulus and damping in soils: Design equations and curves, *ASCE J. Soil Mech. Found. Div.* **98**, no. sm7, 667–692.
- Hartzell, S., L. F. Bonilla, and R. A. Williams (2004). Prediction of nonlinear soil effects, *Bull. Seismol. Soc. Am.* **94**, no. 5, 1609–1629.
- Hartzell, S., D. Carver, R. A. Williams, S. Harmsen, and A. Zerva (2003). Site response, shallow shear-wave velocity, and wave propagation at the San Jose, California, Dense Seismic Array, *Bull. Seismol. Soc. Am.* **93**, no. 1, 443–464.
- Hartzell, S., M. Gatterer, P. M. Mai, P.-C. Liu, and M. Fisk (2005). Calculation of broadband time histories of ground motion, Part II: Kinematic and dynamic modeling using theoretical Green's functions and comparison with the 1994 Northridge earthquake, *Bull. Seismol. Soc. Am.* **95**, no. 2, 614–645.
- Hill, J., H. Benz, M. Murphy, and G. Schuster (1990). Propagation and resonance of *SH* waves in the Salt Lake Valley, Utah, *Bull. Seismol. Soc. Am.* **80**, no. 1, 23–42.
- Holzer, T. L., T. L. Youd, and T. C. Hanks (1989). Dynamics of liquefaction during the 1987 Superstition Hills, California earthquake, *Science* **244**, no. 4900, 56–59.
- Hunter, John D. (2007). Matplotlib: A 2D graphics environment. *Comput. Sci. Eng.* **9**, 90–95.
- Iai, S., Y. Matsunaga, and T. Kameoka (1990a). Parameter identification for a cyclic mobility model, *Rept. Port Harbour Res. Inst.* **29**, 57–83.

- Iai, S., Y. Matsunaga, and T. Kameoka (1990b). Strain space plasticity model for cyclic mobility, *Rept. Port Harbour Res. Inst.* **29**, 27–56.
- Iai, S., T. Morita, T. Kameoka, Y. Matsunaga, and K. Abiko (1995). Response of a dense sand deposit during 1993 Kushiro-Oki earthquake, *Soils Found.* **35**, 115–131.
- Irikura, K., and K. Kamae (1994). Estimation of strong ground motion in broad-frequency band based on a seismic source scaling model and an empirical Green's function technique, *Ann. Geofisc.* **37**, no. 6, 1721–1743.
- Ishihara, K. (1996). *Soil Behaviour in Earthquake Geotechnics*, Clarendon Press, Oxford, UK.
- Ishihara, K., N. Yoshida, and S. Tsujino (1985). Modelling of stress-strain relations of soils in cyclic loading, in *5th International conference on numerical methods in geomechanics*, Nagoya, Japan, 1–5 April 1985, 373–380.
- Jaeger, J. C., N. G. W. Cook, R. W. Zimmerman, and R. W. Zimmerman (2007). *Fundamentals of Rock Mechanics*, Wiley-Blackwell, New York.
- Joyner, W. B., and A. T. F. Chen (1975). Calculation of nonlinear ground response in earthquakes, *Bull. Seismol. Soc. Am.* **65**, no. 5, 1315–1336.
- Kamae, K., K. Irikura, and A. Pitarka (1998). A technique for simulating strong ground motion using hybrid Green's function. *Bull. Seismol. Soc. Am.* **88**, no. 2, 357–367.
- Konno, K., and T. Ohmachi (1998). Ground-motion characteristics estimated from spectral ratio between horizontal and vertical components of microtremor, *Bull. Seismol. Soc. Am.* **88**, no. 1, 228–241.
- Li, X., and Z. Liao (1993). Dynamic skeleton curve of soil stress-strain relation under irregular cyclic loading, *Earthq. Res. China* **7**, 469–477.
- Magistrale, H., K. Olsen, and J. Pechmann (2008). Construction and verification of a Wasatch Front Community Velocity Model: Collaborative Research with San Diego State University and the University of Utah, *U.S. Geol. Surv. Final Tech. Rept.*, National Earthquake Hazards Reduction Program, Award 06HQGR0012.
- Magistrale, H., J. C. Pechmann, and K. B. Olsen (2009). The Wasatch Front, Utah, community seismic velocity model, *Seismol. Res. Lett.* **80**, 368.
- Mai, P. M., and G. C. Beroza (2003). A hybrid method for calculating near-source, broadband seismograms: Application to strong motion prediction, *Phys. Earth Planet. Int.* **137**, 183–199.
- Mai, P. M., W. Imperatori, and K. B. Olsen (2010). Hybrid broadband ground-motion simulations: Combining long-period deterministic synthetics with high-frequency multiple S -to- S backscattering, *Bull. Seismol. Soc. Am.* **100** no. 5A, 2124–2142.
- Masing, G. (1926). Eigenspannungen und Verfestigung beim Messing, in *Proc. 2nd Int. Congress of Applied Mechanics*, Zürich, Switzerland, vol. 332 (in German).
- McCalpin, J., and C. Nelson (2000). Long recurrence records from the Wasatch fault zone, *U.S. Geol. Surv. Final Tech. Rept.*, National Earthquake Hazards Reduction Program, Contract number 99HQGR0058.
- McCalpin, J. P., and S. P. Nishenko (1996). Holocene paleoseismicity, temporal clustering, and probabilities of future large ($M > 7$) earthquakes on the Wasatch fault zone, Utah, *J. Geophys. Res.* **101**, 6233–6253.
- McDonald, G. N., and F. X. Ashland (2008). Earthquake site conditions in the Wasatch Front urban corridor, Utah, *Utah Geol. Surv. Spec. Study* **125**.
- Mena, B., E. Durukal, and M. Erdik (2006). Effectiveness of hybrid Green's function method in the simulation of near-field strong motion: An application to the 2004 Parkfield earthquake, *Bull. Seismol. Soc. Am.* **96**, no. 4B, S183–S205.
- Mena, B., P. M. Mai, K. B. Olsen, M. D. Purvance, and J. N. Brune (2010). Hybrid broadband ground-motion simulation using scattering Green's functions: Application to large-magnitude events, *Bull. Seismol. Soc. Am.* **100**, no. 5A 2143–2162.
- O'Connell, D. R. H., S. Ma, and R. J. Archuleta (2007). Influence of dip and velocity heterogeneity on reverse- and normal-faulting rupture dynamics and near-fault ground motions, *Bull. Seismol. Soc. Am.* **97**, no. 6, 1970–1989.
- Olsen, K. B. (1994). Simulation of three-dimensional wave propagation in the Salt Lake Basin, *Ph.D. Thesis*, University of Utah, Salt Lake City, Utah.
- Olsen, K. B., S. M. Day, L. A. Dalguer, J. Mayhew, Y. Cui, J. Zhu, V. Cruz-Atienza, D. Roten, P. Maechling, T. Jordan, D. Okaya, and A. Chourasia (2009). ShakeOut-D: Ground motion estimates using an ensemble of large earthquakes on the southern San Andreas fault with spontaneous rupture propagation, *Geophys. Res. Lett.* **36**, L04303.
- Pitarka, A., P. Somerville, Y. Fukushima, T. Uetake, and K. Irikura (2000). Simulation of near-fault strong-ground motion using hybrid Green's functions, *Bull. Seismol. Soc. Am.* **90**, no. 3, 566–586.
- Pyke, R. M. (1979). Nonlinear soil models for irregular cyclic loadings, *J. Geotech. Eng. Div.* **105**, no. 6, 715–726.
- Roten, D., D. Fäh, K. B. Olsen, and D. Giardini (2008). A comparison of observed and simulated site response in the Rhône valley, *Geophys. J. Int.* **173**, 958–978.
- Roten, D., D. Fäh, L. F. Bonilla, S. Alvarez-Rubio, T. M. Weber, and J. Laue (2009). Estimation of non-linear site response in a deep Alpine valley, *Geophys. J. Int.* **178**, no. 3, 1597–1613.
- Roten, D., K. B. Olsen, J. C. Pechmann, V. M. Cruz-Atienza, and H. Magistrale (2011). 3D simulations of M 7 earthquakes on the Wasatch fault, Utah, Part I: Long-period (0–1 Hz) ground motion, *Bull. Seismol. Soc. Am.* **101**, no. 5, 2045–2063.
- Schnabel, P., H. B. Seed, and J. Lysmer (1972). Modification of seismograph records for effects of local soil conditions, *Bull. Seismol. Soc. Am.* **62**, no. 6, 1649–1664.
- Silva, W. J., I. G. Wong, and R. B. Darragh (1998). Engineering characterization of earthquake strong ground motions in the Pacific Northwest, in *Assessing Earthquake Hazards and Reducing Risk in the Pacific Northwest*, A. M. Rogers, T. J. Walsh, W. J. Kockleman, and G. R. Priest (Editors), *U.S. Geol. Surv. Profess. Pap. 1560*, vol. **2**, 313–324.
- Solomon, B. J., N. Storey, I. Wong, N. Gregor, D. Wright, and G. McDonald (2004). Earthquake-hazards scenario for a M 7 earthquake on the Salt Lake City segment of the Wasatch fault zone Utah, *Utah Geol. Surv. Spec. Study 111DM*, 59 pp., 6pl.
- Taborda, R., and J. Bielak (2008). Three-dimensional modeling of earthquake ground motion in basins, including nonlinear wave propagation in soils, *U.S. Geol. Surv. Final Tech. Rept.*, Award 08HQGR0018.
- Towhata, I., and K. Ishihara (1985). Modeling soil behavior under principal axes rotation, in *5th International Conf. on Numerical Methods in Geomechanics*, Nagoya, Japan, 1–5 April 1985, 523–530.
- Vucetic, M. (1990). Normalized behavior of clay under irregular cyclic loading, *Can. Geotech. J.* **27**, no. 1, 29–46.
- Vucetic, M., and R. Dobry (1991). Effect of soil plasticity on cyclic response, *J. Geotech. Eng.* **117**, no. 1, 89–107.
- Wessel, P., and W. H. F. Smith (1998). New, improved version of Generic Mapping Tools released, *Eos Trans. AGU* **79**, no. 47, 579.
- Williams, R. A., K. W. King, and J. C. Tinsley (1993). Site response estimates in Salt Lake Valley, Utah, from borehole seismic velocities, *Bull. Seismol. Soc. Am.* **83**, no. 3, 862–889.
- Wong, I., W. Silva, N. Gregor, D. Wright, F. Ashland, G. McDonald, S. Olig, G. Christenson, and B. Solomon (2002). Earthquake scenario ground shaking maps for the central Wasatch Front, Utah, in *Proc. of the 7th U.S. National Conf. on Earthquake Engineering*, Boston, Massachusetts, 21–25 July 2002.
- Wong, I., W. Silva, S. Olig, P. Thomas, D. Wright, N. Ashland, N. Gregor, J. Pechmann, M. Dober, G. Christenson, and R. Gerth (2002). Earthquake scenario and probabilistic ground shaking maps for the Salt Lake City, Utah metropolitan area, *Utah Geol. Surv. Misc. Pub.*, MP-02-5.
- Wong, I. G., W. J. Silva, J. C. Pechmann, R. B. Darragh, and T. Yu (2011). Analyses of earthquake source, path, and site factors from ANSS data

- along the Wasatch Front, Utah, *U.S. Geol. Surv. Final Tech. Rept.*, Award 05HQGR0010.
- Zeghal, M., and A. W. Elgamel (1994). Analysis of site liquefaction using earthquake records, *J. Geotech. Eng.* **120**, no. 6, 996–1017.
- Zeng, Y. (1993). Theory of scattered *P*- and *S*-wave energy in a random isotropic scattering medium, *Bull. Seismol. Soc. Am.* **83**, no. 4, 1264–1276.
- Zeng, Y., J. G. Anderson, and S. Feng (1995). Subevent rake and random scattering effects in realistic ground motion simulation, *Geophys. Res. Lett.* **22**, no. 1, 17–20.
- Zeng, Y., F. Su, and K. Aki (1991). Scattering wave energy propagation in a random isotropic scattering medium 1. Theory, *J. Geophys. Res.* **96**, no. B1, 607–619.

Department of Geological Sciences
San Diego State University
5500 Campanile Dr.
San Diego, California 92182-1020
daniel.roten@sed.ethz.ch
(D.R., K.B.O.)

Department of Geology and Geophysics
University of Utah
115 South 1460 East, Room 383 FASB
Salt Lake City, Utah 84112-0102
(J.C.P.)

Manuscript received 7 October 2011